

ABSTRACT

Title of thesis: MELTING AND PHASE RELATIONS IN IRON-SILICON ALLOYS WITH APPLICATIONS TO THE EARTH'S CORE

Noah Andrew Miller, Master of Science, 2009

Thesis directed by: Professor Andrew J. Campbell
Department of Geology

Experiments were performed on iron-silicon alloys to determine their suitability as analog compositions for the Earth's core. Starting compositions with 9 wt.% silicon and 16 wt.% silicon were compressed in diamond anvil cells and laser-heated. The melting temperatures of the alloys were measured up to 52 GPa using a recently developed optical system. Both curves show a melting point depression from pure iron but intersect at ~50 GPa.

The two starting compositions were also studied up to 90 GPa and over 3500 K in synchrotron x-ray diffraction experiments, and phase diagrams were constructed for both compositions that show significant deviation from the pure iron phase diagram. Based on this synchrotron data, a model was produced which predicts the core to contain 8.6 to 11.1 wt.% silicon for a core-mantle boundary temperature of 4000 K.

MELTING AND PHASE RELATIONS IN IRON-SILICON ALLOYS
WITH APPLICATIONS TO THE EARTH'S CORE

by

Noah Andrew Miller

Thesis submitted to the Faculty of the Graduate School of the
University of Maryland, College Park in partial fulfillment
of the requirements for the degree of
Master of Science
2009

Advisory Committee:

Professor Andrew J. Campbell, Chair
Professor Saswata Hier-Majumder
Professor William F. McDonough

Acknowledgements

I would like to acknowledge the support of my advisor, Andy Campbell, as well as my committee members Bill McDonough and Sash Hier-Majumder. I also wish to thank Greg Shofner, Rebecca Fischer, Chris Seagle (University of Chicago) and Vitali Prakapenka (GSECARS) for their help in the preparation and execution of the experiments, and Oluchi Ofoha for assistance with data analysis.

Contents

List of Tables	iv
List of Figures	v
1. Introduction	1
1.1. Formation and Significance of the Core	2
1.2. Density of the Core	4
1.3. The Light Element Contribution	6
1.4. Previous Studies	8
1.4.1. Studies of Pure Iron	8
1.4.2. Studies of Iron-Silicon Alloys	10
1.5. This Study	19
2. Methods	21
2.1. Diamond Anvil Cell Sample Preparation	21
2.2. Optical Experiments	27
2.2.1. Pressure Measurement	27
2.2.2. Laser-Heating and Temperature Measurement	29
2.3. X-Ray Diffraction Methods	34
2.3.1. Pressure Measurement	34
2.3.2. Laser-Heating and Temperature Measurement	36
2.3.3. Analysis of X-Ray Diffraction Patterns	37
3. Results	39
3.1. Optically Determined Melting Curves	39
3.2. X-Ray Diffraction Results	41
3.3. Calculations of Atomic Density	53
4. Discussion	56
4.1. Optical Melting Curves	56
4.2. The Fe-9Si and Fe-16Si Phase Diagrams	57
4.3. XRD Melting Data	58
4.4. The B2 Phase	61
4.5. Silicon and the Core Density Deficit	62
4.6. Application to the Core	67
4.7. Future Work	68
5. Conclusions	70
6. Appendix	71
7. References	75

List of Tables

1. Electron Microprobe Analyses of 9 wt.% Silicon Starting Materials	25
2. Electron Microprobe Analyses of 16 wt.% Silicon Starting Materials	26
3. Thermal Pressure as a Result of Laser-Heating	28
4. Melting Temperatures of Iron-Silicon Alloys	40
5. Measured Pressures and Temperatures for the HCP-FCC Transition	44
6. Phases Determined in XRD Analyses	45
7. d-Spacings of Phase X	52

List of Figures

1. Phase diagram of pure iron	9
2. Phase diagram of the Fe-Si system at 1 bar	11
3. Phase diagrams of Fe-Si alloy containing 8 wt.% Si from Lin et al.(2002)	13
4. Phase diagram of Fe-Si alloy containing 8 wt.% Si from Lin et al.(2009)	15
5. Phase diagram of FeSi _{3.4}	16
6. Solubility of silicon in FCC iron	17
7. CALPHAD phase diagrams from Brosh et al. (2009)	18
8. Cross-section of a diamond anvil cell	23
9. 2-D Temperature plot for sample N38-4	31
10. Plots of emissivity vs temperature, samples N38-4 and N59-3	33
11. 2-D and integrated X-ray diffraction patterns for sample Si9-104	38
12. Melting temperatures of Fe-9Si and Fe-16Si	39
13. X-ray diffraction pattern for sample Si9_354	42
14. FCC-HCP transition in pure iron	43
15. Phase diagram for Fe-9Si	46
16. Demonstration of ordering between the BCC and B2 structures	47
17. X-ray diffraction pattern for sample Si9_386 showing melt	48
18. Phase diagram for Fe-16Si	50
19. X-ray diffraction pattern for sample Si16_012 showing Phase X	51
20. Density of Fe-16Si vs. pressure	54
21. Comparison of atomic volumes of iron-silicon alloys to pure iron	55
22. Density of liquid iron in the outer core	64

23. Amount of Si needed to account for the density deficit vs. CMB temperature	65
24. Error calculation for Figure 23	66

1. Introduction

The Earth's core comprises one third of the planet's mass and is composed mostly of iron. There are two layers within the core: a solid inner core surrounded by a shell of molten material. The outer core contacts the base of the mantle at approximately 2900 km below the Earth's surface, a depth that renders direct sampling of the core's material impossible. Consequently, many questions remain unsolved regarding the core's composition and physical properties.

The composition of the core is poorly constrained, and the crystal structure of the inner core is unknown. This study will contribute to the understanding of these two related issues by examining silicon's effect on the phase diagram of iron at high pressures and temperatures.

Samples of Fe-Si alloys were compressed in diamond anvil cells and heated with a laser until they melted. This experimental method allowed observation of the behavior and structure of materials under deep-Earth conditions. Although the pressures in the Earth's core are significantly higher than those reached in this study, the results obtained allow some extrapolation to core conditions.

The data obtained place new constraints on the composition of the Earth's core. It is known that the core contains several percent of element(s) lighter than iron and that the outer core contains a higher proportion of light elements than the inner core (Birch, 1966). The temperatures at the core-mantle boundary (CMB) and the inner core-outer core boundary (ICB) are poorly constrained. If silicon is accepted as a component of the core on the level of several percent, these experiments help to constrain that temperature range and thermal structure of the core.

1.1. Formation and Significance of the Core

The Earth's core remains the most inaccessible region of the planet many decades after its discovery. The nature of the crust and mantle is largely known through seismology and mantle xenoliths; the composition of basalts, particularly intraplate lavas from Hawaii, also provides chemical information on depths that may reach down to the core-mantle boundary. However, no tangible evidence of the core's composition has presented itself, so geologists are left largely with seismological studies which describe the core's physical properties. Comparisons between the composition of the bulk Earth and that of chondrites provides more information, but the concentration of volatile elements in the Earth remains poorly constrained as long as the process of the Earth's accretion is poorly understood.

Despite the difficulties involved in studying the Earth's innermost layers, there are numerous reasons for doing so. To understand the nature of the core is, in a large sense, to understand the processes that lead to the formation of the planet as it exists today. Based on observations from the most primitive chondrites, the Earth was originally comprised of undifferentiated masses of metal and silicate rock. The processes of accretion and core differentiation are much debated (Righter et al, 1997; Rubie et al., 2003), with the disagreements largely focused on the pressure, temperature and redox conditions of core segregation.

Even if these factors were known precisely, they would still not give a complete picture of the core's formation. There are multiple explanations of how the metallic part of the primitive Earth physically separated from the silicate part and gravitationally settled to the center of the planet. It has been suggested that the metallic portion of the

primitive Earth collected at the base of a differentiating magma ocean, which would necessitate chemical equilibrium at corresponding pressures and temperatures (Corgne et al., 2008; Lee et al., 2007; Wood et al., 2007). The depth of this magma ocean is unresolved, but at some point there would have occurred a density inversion in which the metallic melt would have gravitationally settled to the center of the planet. Alternatively, it is possible that droplets of molten metal gradually fell towards the center of the Earth (e.g. Yoshino et al., 2004). Either mechanism would lead to very different conditions of metal-silicate equilibration and potentially very different partitioning of elements into the core.

In addition, it is unclear how the formation of the Moon affected the Earth's differentiation process. The currently dominant model of lunar formation involves a Mars-sized object impacting the Earth at an oblique angle; the resulting debris coalesced in orbit around the Earth to form the Moon. The core of the impactor merged with that of the Earth (Canup and Asphaug, 2001), which explains the lack of a lunar core. If this model is correct, then the core's composition is comprised of two mixed reservoirs which may be chemically impossible to distinguish from each other after billions of years of mixing.

Another reason to study the Earth's core is that it houses the mechanism that creates the planet's magnetic field (Stevenson, 2003). Convection currents within the outer core are likely induced by chemical differences between the compositionally light outer core and denser inner core (Jeanloz, 1987). As iron-rich crystals freeze onto the inner core, the relatively buoyant, iron-poor liquid rises towards the mantle.

1.2. Density of the Core

The core has long been known to consist primarily of iron with several weight percent of nickel. This is based on the composition of chondrites - early, undifferentiated materials of the solar system. The low volatility of both those elements, combined with reasonable constraints on their concentrations in the crust and mantle, suggests that their proportions in the core can be accurately determined from chondrite studies. Because the addition of several weight percent nickel has a negligible effect on the density of iron (Shanker et al., 2004), most experimenters have used pure iron as a substitute for an iron-nickel alloy when attempting to replicate conditions in the Earth's core.

Seismological studies have provided a range of information about the core, including its density. The PREM model of Dziewonski and Anderson (1981) combines a range of seismic data to give densities for the outer core of 9900 to 12100 kg/m³ and 12800 to 13100 kg/m³ for the inner core. These values are reasonably well constrained and have not changed greatly since their publication. Masters and Gubbins (2003) calculated an 820 ± 180 kg/m³ jump in density at the inner core-outer core boundary (ICB) based on seismic data. While this is a larger jump than estimated by the PREM model, it does not greatly affect the interpretation of recent Fe-density studies because the density of pure iron (or a similar Fe-Ni alloy) at core conditions has always been much harder to resolve.

The difficulty in estimating the density of iron at several hundred GPa is due partly to the experimental difficulties involved in reaching such high pressures, and partly to the wide range of temperatures that have been proposed for the core. Very few

studies have reached pressures comparable to those in the inner core, and so extrapolation from lower pressures is often necessary. This extrapolation is possible as long as an accurate equation of state exists for iron; while an equation of state nominally allows for the extrapolation of density, this extrapolation also allows the determination of other properties such as seismic parameters. As will be discussed, there is considerable debate over which structure of iron exists at extremely high pressures and which phases are stabilized by the addition of other elements.

Regardless of the precise density of iron at high pressure and temperature, there is general agreement that iron at core conditions is denser than the core itself. Numerous authors have put forward approximations of the density deficit, most of which range from 5 to 15%. Birch (1952) suggested that there was a 20% difference between room-temperature iron at core pressure and the core itself; this difference was lessened to 10% for iron at high temperatures, and the real value was considered to be somewhere in between those values. Knopoff and MacDonald (1960) used shock experiments to verify Birch's 20% deficit for cold Fe; they suggested a lesser temperature contribution, however, and concluded a value of 14-15% for the density deficit at high temperature. McQueen and Marsh (1966) concluded an 8% deficit based on shock data on iron and Fe-Ni, while Brown and McQueen (1982) measured 5-7% for pure iron. Anderson and Ahrens (1994) concluded a 5-10% deficit for an inner/outer core boundary temperature between 5000 and 8000 K based on the equation of state of liquid iron. Anderson and Isaak (2002) used a similar technique to conclude a deficit of 3.8 to 7%, while Shanker et al. (2004) reach a value of ~10% by using a revised bulk modulus. The wide range in estimates results partly from uncertainty in the pressure

derivative of the bulk modulus; recent values from Dewaele et al. (2006) are 163.4 ± 7.9 GPa for the bulk modulus and 5.38 ± 0.16 for its pressure derivative.

Jephcoat and Olson (1987) explored the possibility that the density deficit could be due to an inaccurate coefficient of thermal expansion of iron. If the core were comprised of pure iron, it would require a coefficient five times larger than previous estimates to account for the density deficit by thermal expansion alone. Consequently, Jephcoat and Olson (1987) concluded that a more reasonable explanation for the deficit is that the core contains one or more elements lighter than iron.

Some authors have assumed that the density deficit is a result only of a difference in mean atomic number between the core and pure iron. McDonough (2003) and Birch (1966) both assumed a mean atomic number of ~ 23 when calculating compositions for the core.

1.3. The Light Element Contribution

In order to account for the density deficit, there must be an additional element present in the core which is significantly lighter than iron. Carbon, oxygen, silicon, sulfur, hydrogen, phosphorus, and nitrogen have each been proposed, and some have been discounted over time as geochemically unfeasible. It was suggested by Wood (1993) that carbon is sufficiently soluble in iron at high pressure to allow its incorporation into the core. However, comparison of the Earth's mantle to carbonaceous chondrites indicates that the concentration of carbon in the core is limited to ~ 0.2 wt% (McDonough, 2003). There is simply not enough carbon in the materials from which the Earth is derived to account for the density deficit. McDonough (2003)

derives the same value for the concentration of phosphorus in the core based on the same reasoning. In other words, there is not nearly enough carbon or phosphorus in the bulk Earth to satisfy the density deficit.

A similar conclusion must be drawn for sulfur, though for a different reason. As a volatile element, the concentration of sulfur in the Earth cannot be directly related to the concentration of sulfur in chondrites, but its volatility relative to other elements can be calculated if the outer core contained 10% sulfur. As demonstrated by Dreibus and Palme (1996), there would have to be considerably more S in the bulk silicate Earth than can be accounted for if sulfur were present in the core in any great amount. The maximum calculated sulfur content of the core is ~ 1.7 wt%, which is comparable to calculations of 1.5 to 2 wt% McDonough (2003) and 2.3 wt% (Allegre et al., 1995) but these concentrations are not enough to account for the density deficit. Hydrogen and nitrogen are generally left out of core composition models due to their high volatility (e.g. Badro et al., 2007).

The remaining two elements, oxygen and silicon, are both strong candidates for the light element contribution with no overwhelming drawbacks. Both are present in excess in the silicate Earth and soluble in liquid iron. Although the solubility of oxygen in iron increases with temperature, O'Neill et al. (1998) found that it decreases with pressure to the point that only $\sim 2\%$ oxygen could be found in the core. This conclusion was revised by Ozawa et al. (2008), who found that oxygen solubility had negligible pressure dependence above 38 GPa, allowing up to 8% oxygen in the core. While Asahara et al. (2007) reported a more substantial pressure dependence, they also reported an 8-10 wt% maximum oxygen concentration in the outer core. This amount

could potentially account for the Fe-density deficit. Seagle et al. (2008) conclude that oxygen could be a major component in the core for several reasons: it depresses the melting point of iron and it preferentially goes into the liquid phase during melting. Seagle et al. (2008) estimate that 9 wt% oxygen would be necessary to account for the density deficit in the outer core.

Authors have proposed compositions for the Earth's core based on geochemical evidence. McDonough (2003) proposed two compositions, one containing silicon and one containing oxygen. Such multi-element compositions are important to consider; however, it is important to gain a thorough understanding of the Fe-Si system before attempting to tackle more complicated multi-phase systems.

1.4. Previous Studies

While some work has been performed attempting to understand the Fe-Si system, no previous experiments have completed the phase diagram in pressure-temperature-composition (P-T-X) space to any considerable extent. Because the core contains roughly an order of magnitude more iron than silicon (e.g. McDonough, 2003), it is reasonable to constrain experiments for this study towards Fe-rich compositions.

1.4.1. Studies of Pure Iron

It is reasonable to assume that the Fe-Si phase diagram is essentially a modification of the pure iron diagram such as those described by Boehler (1986), Mao et al. (1987), Shen et al. (1998), and Andraut et al. (2000). Shen et al. (1998), who

measured the stability of iron structures up to 80 GPa, showed four separate fields below the melting curve (Figure 1). At pressures less than ~8 GPa and temperatures below ~700 K, iron exists as a body-centered cubic (BCC) structure. This structure reappears at similar pressures just below the melting curve. At pressures up to 60 GPa and at a temperature which increases with pressure, iron exists as a face-centered cubic (FCC) structure. At high enough pressures, both the BCC and FCC structures transform into the hexagonal close-packed (HCP) structure. Some authors, such as Andrault (2000), show an orthorhombic phase at high pressures above ~1500 K; since this phase has not been reproduced in recent experiments, its existence is suspect.

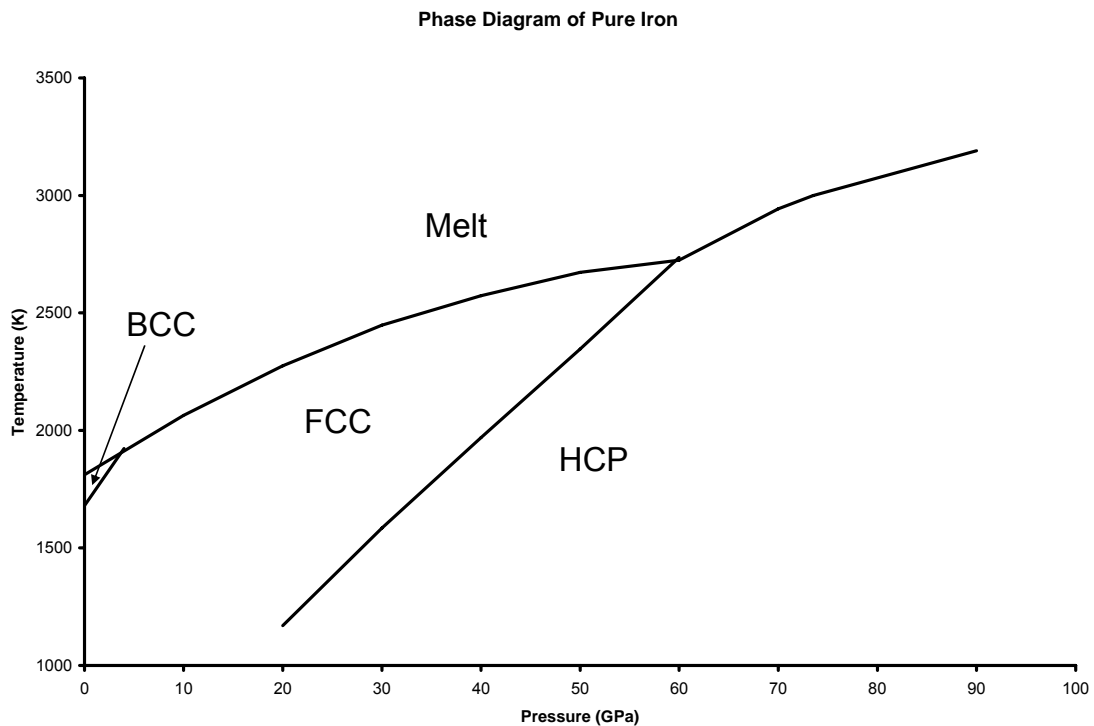


Figure 1. Phase diagram of pure iron after Shen et al. (1998). The various structures are discussed in the text.

While Andraut (2000) and others have suggested that the HCP structure is stable all the way to core pressures, others have argued that the BCC structure becomes stable again at high pressures. Belonoshko et al. (2003) concluded from molecular dynamics simulations that the BCC phase reappears at approximately 100 GPa and remains stable to the center of the core (360 GPa). That paper re-interprets the melting curve of Boehler (1993) as the solid-solid transition between BCC (higher temperature) and HCP (lower temperature). The melting temperature of pure iron was found to be 6300-6600 K at 323.5 GPa. Vocadlo et al. (2003) derived similar results from a quantum mechanical study of the two structures. However, these authors note that the inner core is not pure iron due to the previously described density deficit, and therefore there it is possible that the addition of a minor element could favor the crystallization of a BCC structure. Various authors, such as Belonoshko et al. (2008), have also concluded that a strained BCC structure in the inner core would explain the observed seismic anisotropy better than the HCP structure.

1.4.2. Studies of Iron-Silicon Alloys

Phase diagrams have been constructed for iron-silicon alloys both at one bar and at high pressure. The atmospheric-pressure iron-silicon temperature-composition (T-X) diagram described by Massalski (1986) is shown in Figure 2. There are approximately 11 sub-liquidus stability fields in the 5-15 wt% silicon range, depending on if one considers transitions in magnetism and atomic ordering. The liquidus is depressed compared to the pure-Fe melting point (1811 K) by approximately 150 K for 9 wt% silicon and 250 K for 16 wt% silicon.

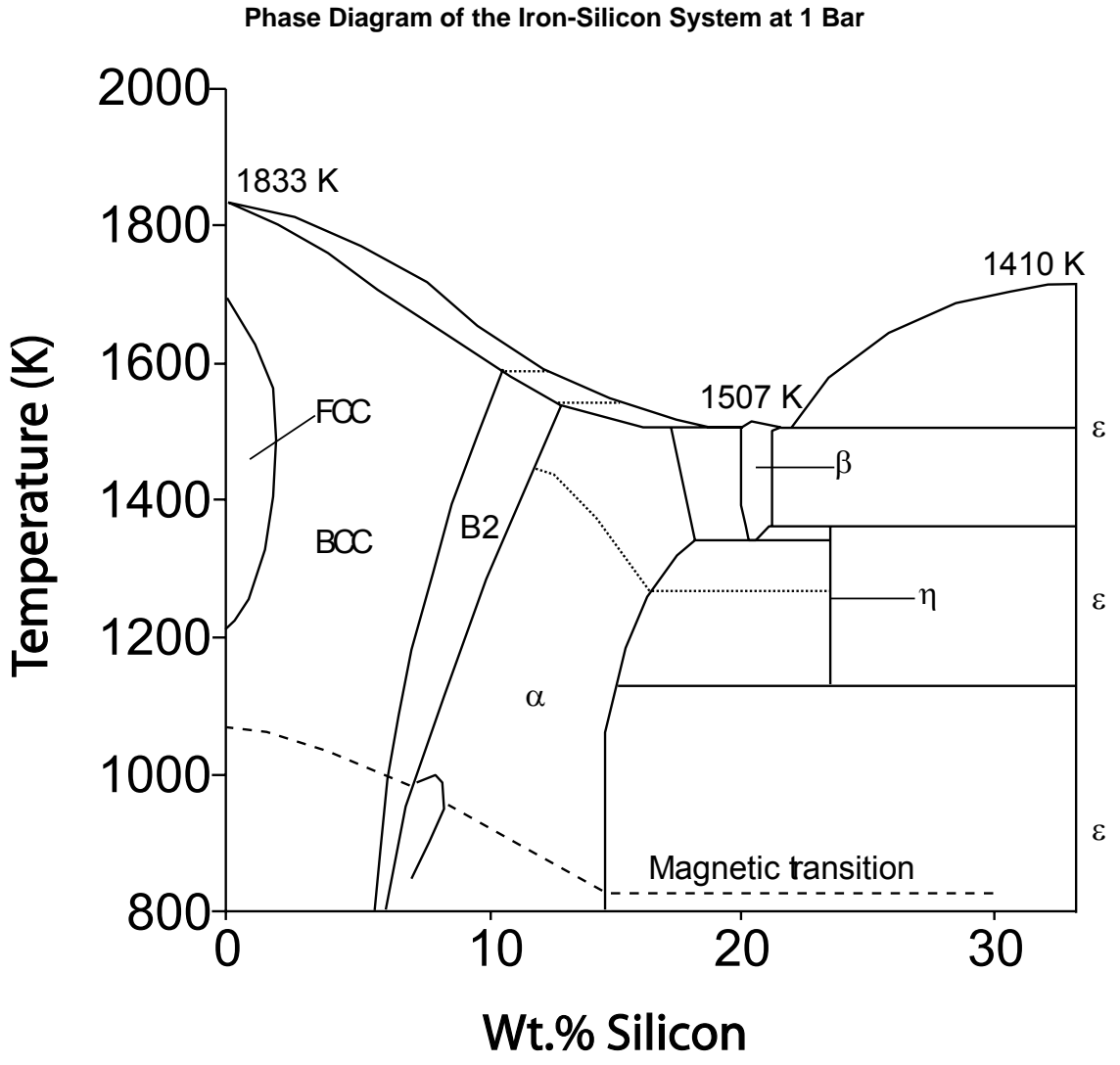
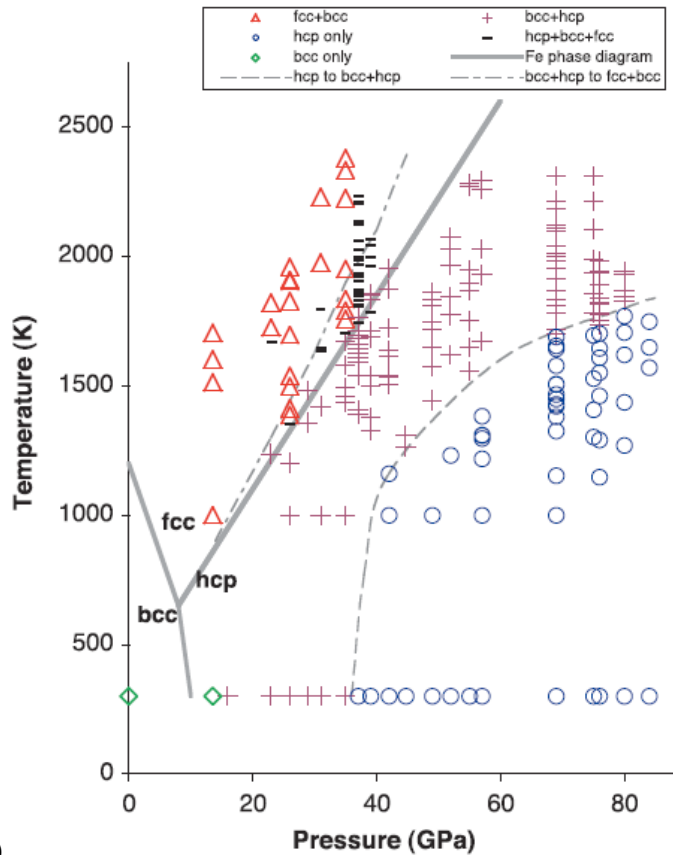
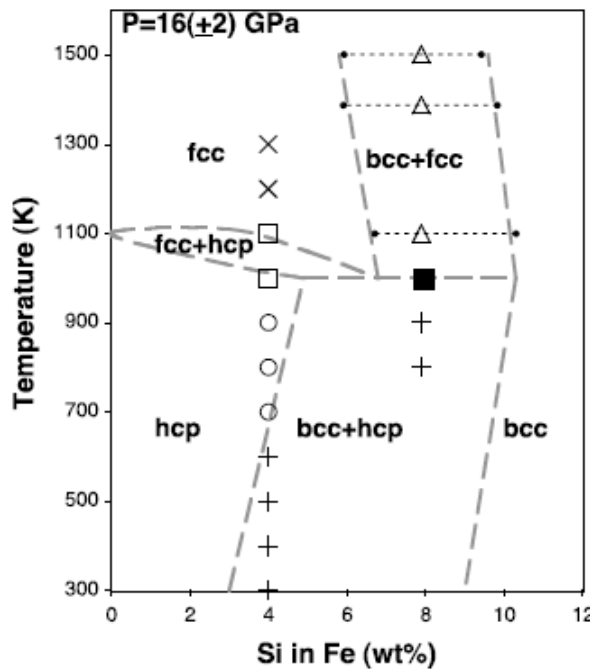


Figure 2. Phase diagram of the Fe-Si system at 1 bar after Massalski (1986). The FCC, BCC and B2 structures are discussed in the text; α is the BiF_3 structure, β is the Fe_2Si structure, ϵ is the FeSi structure and η is the Mn_5Si_3 structure. Uncertain transitions are dotted.

Various experimenters have taken different approaches to produce iron-silicon phase diagrams at high pressure. Kuwayama and Hirose (2004) ran a series of multi-anvil press experiments at 21 GPa and found a single sub-solidus phase existing up to 25 wt% silicon. The temperature range between the liquidus and solidus is very small, less than 50 K at 16 wt% silicon. The solidus temperature of 16 wt% silicon alloy is depressed approximately 50 K from the pure iron melting curve of Shen et al.'s (1998), while the solidus for 9 wt% silicon is slightly higher than that curve. Melting was defined by quench textures using backscatter electron imaging. Lin et al. (2002) shows a very different T-X diagram at 16 GPa based on diamond anvil cell and multi-anvil press experiments (Figure 3). Between 0 and 10 wt% silicon there exist an HCP field and a BCC + HCP field below 1000 K, as well as FCC, FCC + HCP and BCC + FCC fields above that temperature. No melting temperatures are reported. However, a pressure-temperature (P-T) diagram is constructed for 7.9 wt% silicon showing stabilization of the BCC structure with either FCC or HCP to at least 80 GPa and close to 2500 K. There is no upper temperature bound drawn for the BCC phase, giving support to the modeling studies of Belonoshko et al. (2003) and Vocadlo et al. (2003) by suggesting the stability of the structure to very high pressures.



A)



B)

Figure 3. Phase diagrams from Lin et al. (2002). **A.** Phase diagram for Fe-7.9Si in P-T space. **B.**

Phase diagram for varying compositions at 16 GPa. Crosses show BCC+HCP; circles show HCP only; open squares show DCC+HCP; filled squares show BCC+FCC+HCP; triangles show BCC+FCC.

Lin et al. (2009) produced a P-T phase diagram for 7.9 wt% silicon between 100 GPa and 240 GPa (Figure 4). This diagram shows only HCP at low temperatures and a combination of HCP and BCC to at least 150 GPa and 3000 K. This appears to be the highest pressure reached in a static experiment involving an Fe-Si alloy. Figure 4 supports the hypothesis that BCC is present in the core.

Asanuma et al. (2008) carried out diamond anvil cell experiments to over 250 GPa on Fe-alloy containing 3.4 wt% silicon (Figure 5). That study reported expansion of the FCC field to at least 120 GPa at high temperatures but only the HCP structure above 150 GPa. No additional melting data was presented. Zhang and Guyot (1999) focused on lower pressure and temperature phase transitions in multi-anvil press experiments. In particular, they determined the maximum solubility of silicon in the FCC iron structure at 800-1000°C (Figure 6).

Brosh et al. (2009) calculated a phase diagram for Fe-Si alloys containing up to 50% (atomic) silicon. The model was calculated using the free energies of each phase to determine which one(s) are dominant at a given pressure, temperature and composition. The resulting diagram (Figure 7) indicates that at 4 wt% silicon the alloy takes a combination of BCC and HCP at all temperatures between 100 GPa and 200GPa. Above 250 GPa, the structure reverts to only HCP. At 8 wt% silicon the alloy takes a combination of BCC and HCP to at least 300 GPa at all temperatures, suggesting that the addition of greater amounts of silicon further stabilizes the BCC structure. Melt phases were not considered, and thus no melting curves are shown.

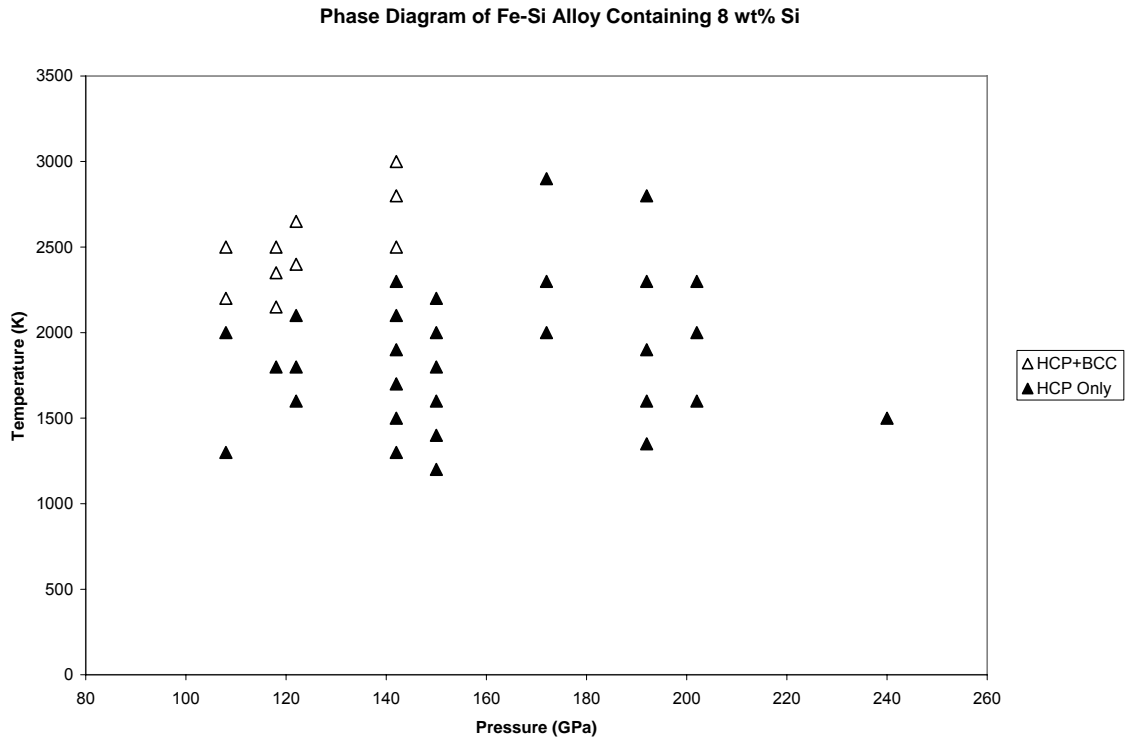
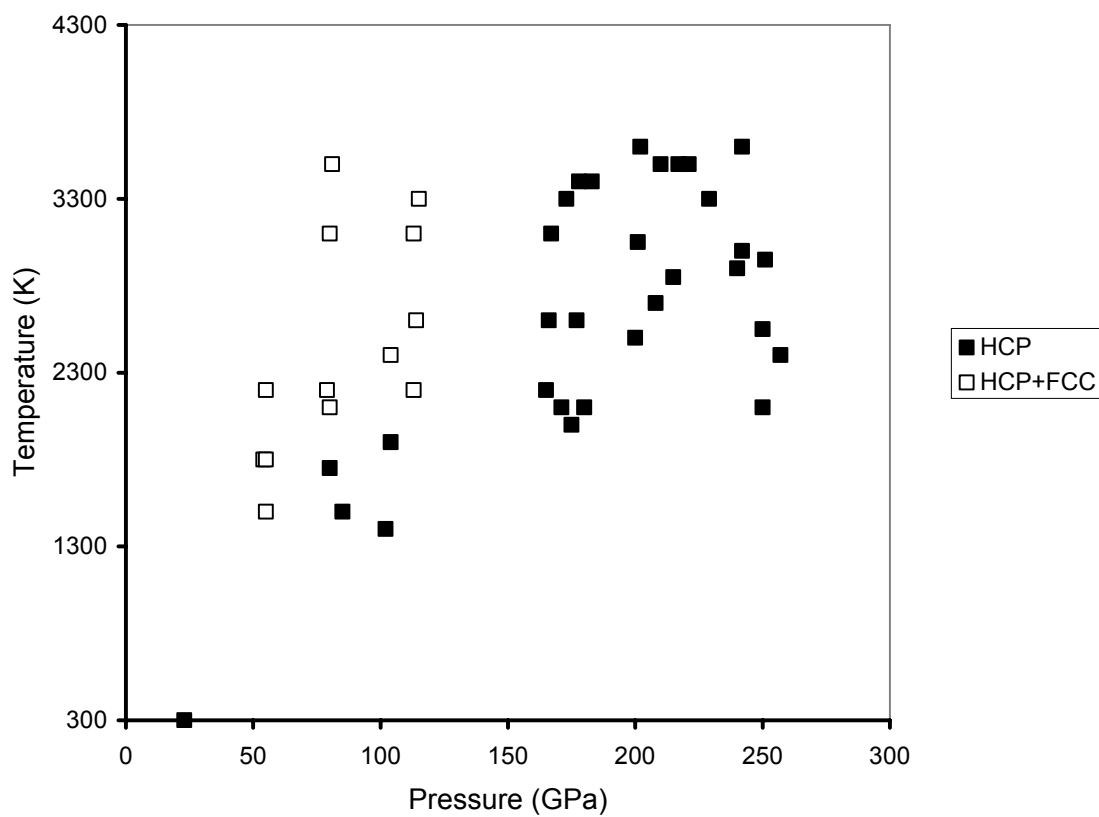


Figure 4. Data from Lin et al. (2009) showing the crystal structure of an Fe-Si alloy containing 8 wt% silicon. The BCC structure is stabilized at high temperature, as suggested by Belonoshko et al. (2003).

Phase Diagram of 3.4 Wt.% Silicon



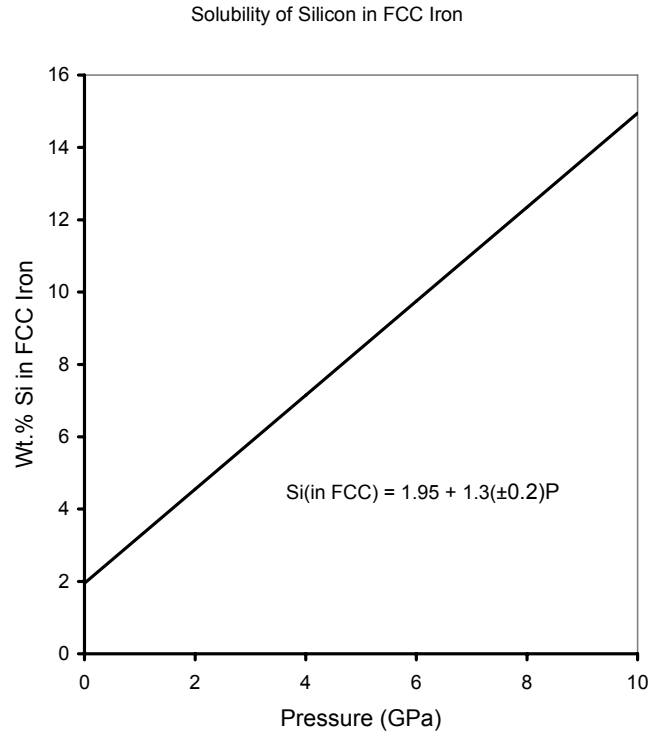


Figure 6. Diagram from Zhang and Guyot (1999) showing maximum solubility of silicon in the FCC phase. Filled triangles show FCC; open triangles show no FCC.

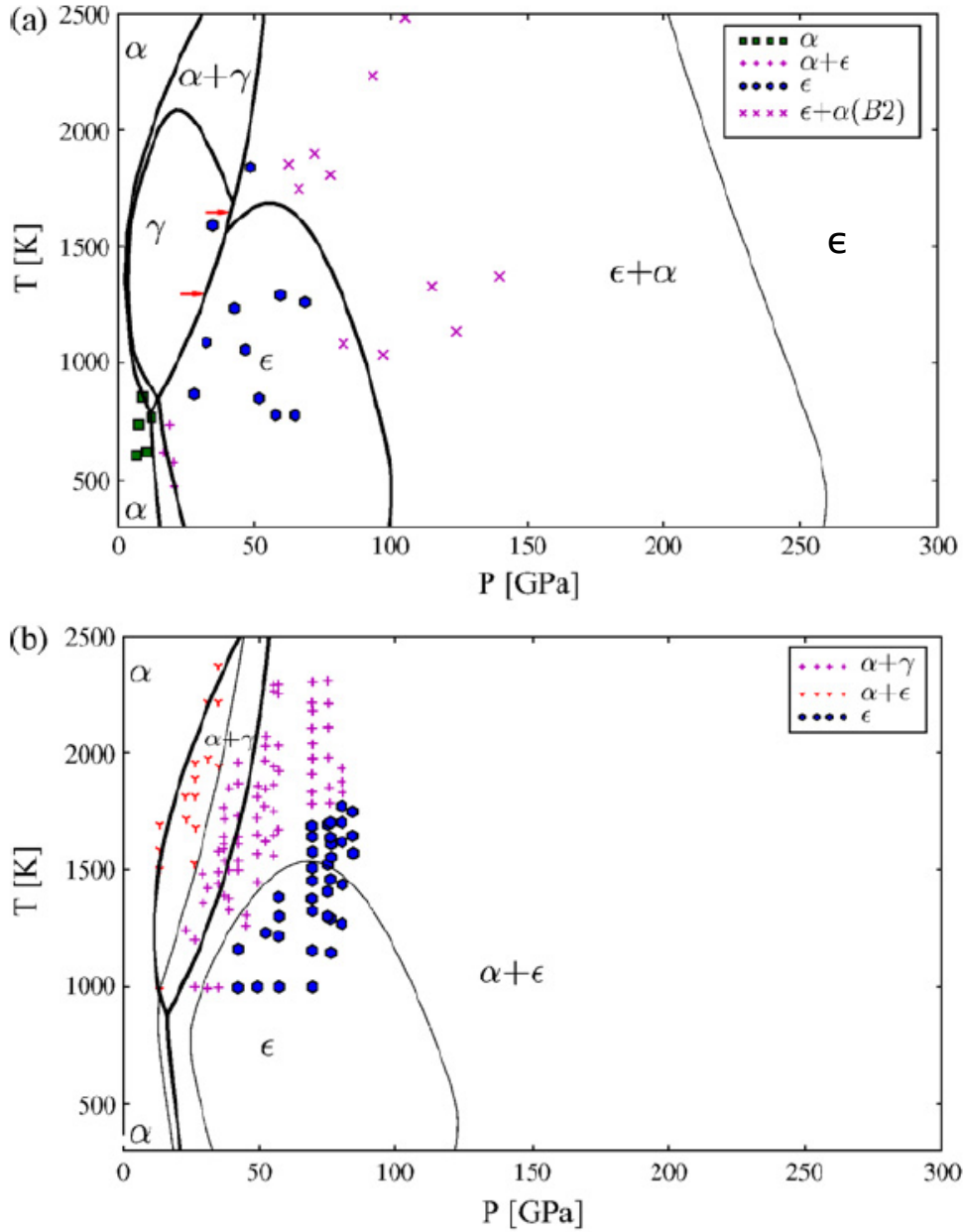


Figure 7. CALPHAD phase diagrams from Brosh et al. (2009). **A)** P-T plot for Fe-Si alloy with 4 wt% silicon. α -Fe is BCC, γ -Fe is FCC and ϵ -Fe is HCP. The B2 structure is a higher ordering of the BCC structure. The red arrows indicate a very small FCC+HCP region. **B)** P-T plot for Fe-Si Alloy with 8 wt% silicon.

1.5. This Study

Significant gaps remain in published data regarding Fe-Si alloys. Lin (2002, 2009) and Asanuma et al. (2008) did not produce melting curves, and a melt phase was not considered in the calculations of Brosh et al. (2009). Kuwayama and Hirose (2004) produced melting data for compositions ranging from pure iron to FeSi, but only at 21 GPa. No P-T phase diagrams have been published for Fe-Si alloys with more than 9 wt.% silicon, and melting data for all compositions is limited.

This study was designed to fill in these gaps. Sub-solidus phase relations and melting curves were obtained for alloys with 9 wt.% and 16 wt.% silicon. There is some overlap with previously published data for 9 wt.% silicon, but, as will be shown, this study provides important corrections to the phase diagram of Lin et al. (2002). Alloys containing 16 wt.% silicon have been only minimally studied before, so the phase diagram produced for that composition is almost completely new. This study also provides new information on the compressibility of iron and silicon atoms; this data, as will be shown, justifies the assumption made by various authors (e.g. McDonough, 2003; Birch, 1966) that the density deficit can be accurately modeled as a difference in the core's mean atomic weight.

Two compositions of iron-silicon alloy, containing 9 wt.% silicon and 16 wt.% silicon, were studied to represent a broad range of possible core compositions. Previous studies have focused on compositions containing less than 9 wt.% silicon (Brosh et al, 2009; Asanuma et al, 2008; Lin et al, 2002; 2009). Data from the 9 wt.% Si alloy were expected to repeat and expand upon the results of Lin et al. (2002, 2009), demonstrating that data from this study can be reproduced by other authors. The 16

wt.% Si composition was chosen to expand the range of published data to a composition above 10 wt.% silicon, because some studies have proposed such higher silicon contents in Earth's core (e.g., MacDonald and Knopoff, 1958).

2. Methods

In order to approximate conditions in the Earth's core, Fe-Si alloys were compressed to high pressures and heated above the melting point. The high pressures are achieved in a diamond anvil cell; while the sample size is limited in this device, the pressure is theoretically limited only by the strength of the anvils and the diamond cell. Samples are heated using an infra-red laser; the pressure and temperature of the sample were measured radiometrically.

Two sets of experiments were performed: melting curves were measured at the University of Maryland using optical techniques developed by Campbell (2008), and sub-solidus and melting information was obtained using synchrotron X-ray diffraction at the Advanced Photon Source (APS), Argonne National Laboratory. Techniques described by Campbell (2008) allow 2-dimensional temperature and emissivity data to be gathered from the laser-heated spot, and melting temperatures can be calculated from this data. For information on sub-solidus phases and the transitions between them, synchrotron X-ray diffraction techniques provide data about the crystal structure of the sample. All of these techniques allow data to be gathered from the sample while it is at simultaneous high pressure and temperature.

2.1. Diamond Anvil Cell Sample Preparation

An analog to deep-Earth conditions can be physically simulated by compressing materials to extremely high pressures. This is difficult for several reasons. First, the amount of force required to reach a certain pressure is inversely proportional to the area over which that force is applied. Thus, larger samples require a greater applied force to

reach a particular pressure, which requires a stronger apparatus and smaller samples. Second, devices must be used which can withstand high pressures. There are few materials that can withstand extremely high pressures without changing their crystal structure or undergoing significant deformation, and those that can are often expensive. Third, to reach high pressures, a sample must be completely enclosed to prevent it from flowing out of a sample chamber. This limits the optical accessibility of the sample unless the sample chamber is bounded by a transparent material, such as diamond. The high temperatures required for constructing a core analog further complicate each of these issues.

Samples were compressed in diamond anvil cells (a cross section of a loaded cell is shown in Figure 8). The samples were 5-10 microns thick and much less than one millimeter in diameter. The culet faces of the diamonds, which form the top and bottom of the sample chamber, were 250, 300 and 400 microns in diameter. The sample chamber was approximately 1/3 the diameter of the culet face and was estimated to be 20-30 microns thick, depending on pressure and the gasket material.

A gasket is created by indenting a metal sheet (steel at UMD, rhenium at APS) to ~20 GPa and using an electronic discharge machine to create a hole in the indentation. The side of this hole forms the wall of the sample chamber. The gasket sits between the diamonds, which formed the top and bottom of the sample chamber. The seal between the diamonds and the gasket becomes airtight at well below 1 GPa, ensuring that no matter can enter or leave the sample chamber during an experiment. The diamonds' transparency to a wide range of wavelengths of light allows for optical observation of the sample as well as X-ray diffraction studies. High temperatures can

be achieved in the cell either through resistive heating or through laser heating, in which a high-intensity laser beam is directed through one or both of the diamond anvils to the sample.

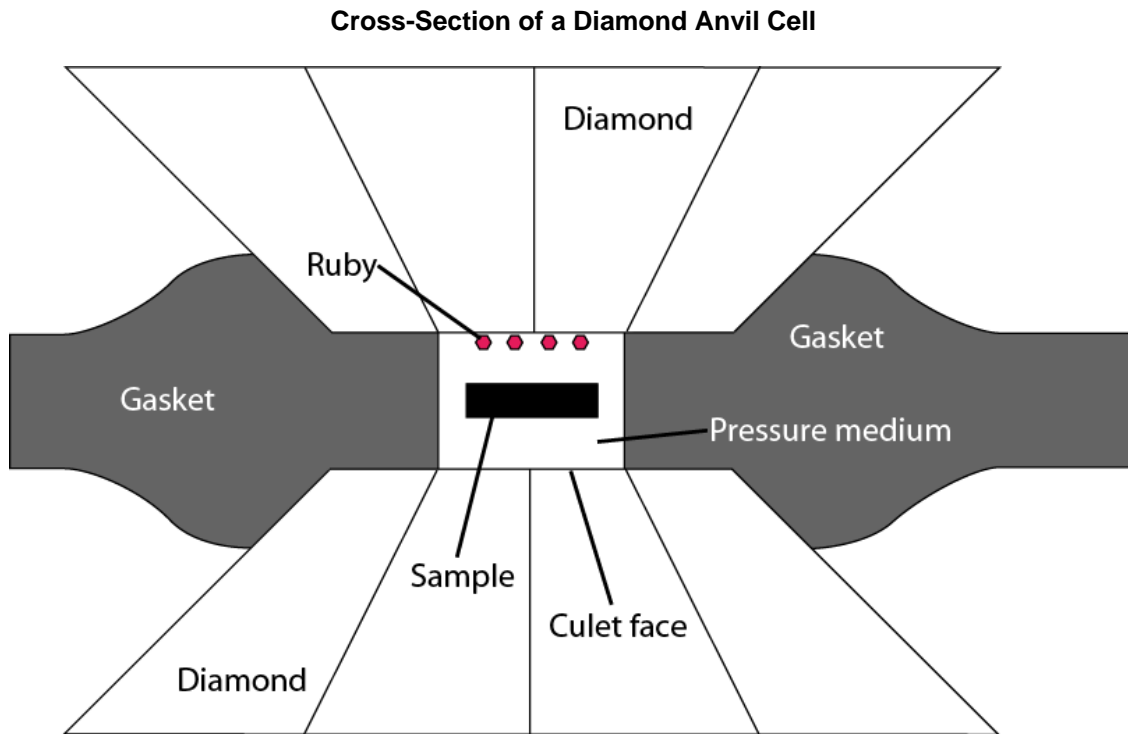


Figure 8. Cross-section of a loaded diamond anvil cell. Not to scale; however, diamond culet faces were 250-400 μm in diameter, and sample chambers were approximately one third the diameter of the culet faces.

Homogeneous iron-silicon alloys of known composition were used as starting materials. A sample of each starting alloy was analyzed by electron microprobe (Tables 1 and 2). The microprobe results show that the alloy described as having 9% silicon contained $8.75 \pm 0.40\%$ Si, and the alloy described as having 16% silicon contained $15.83 \pm 0.26\%$ Si. Both compositions contained trace amounts of chromium, manganese and aluminum; these elements might have been present when the starting materials were created, and they could be contaminants from the laboratory. The total compositions reported by the microprobe average below 99%; this is possibly due to an imperfect polish on the sample analyzed by the microprobe. The 9% alloy was obtained pre-fabricated from Goodfellow Cambridge Limited. The 16% alloy was obtained from Prof. Dion Heinz at the University of Chicago and was synthesized by Prof. William A. Bassett at Cornell University. Both starting compositions were true alloys, not mixtures of materials.

Electron Microprobe Analyses of 9 wt.% Silicon Starting Materials

Wt.%,	Uncorrected					Total
	Al	Fe	Si	Cr	Mn	
	0.00	89.64	8.50	0.12	0.16	98.42
	0.00	84.26	8.04	0.05	0.16	92.50
	0.00	90.14	8.53	0.10	0.19	98.96
	0.00	89.64	8.54	0.17	0.21	98.56
	0.01	89.26	8.81	0.12	0.16	98.36
	0.00	90.01	7.69	0.11	0.16	97.97
	0.00	89.56	9.27	0.07	0.17	99.07
	0.00	88.50	8.91	0.04	0.17	97.62
	0.02	88.57	8.43	0.03	0.17	97.22
	0.00	88.16	8.64	0.04	0.13	96.97
Average:	0.00	88.77	8.54	0.08	0.17	97.57
			Corrected (Total = 100%)			
	0.00	91.08	8.64	0.12	0.16	100
	0.00	91.09	8.69	0.05	0.17	100
	0.00	91.08	8.62	0.10	0.19	100
	0.00	90.95	8.66	0.17	0.21	100
	0.01	90.74	8.96	0.12	0.17	100
	0.00	91.88	7.85	0.11	0.16	100
	0.00	90.40	9.36	0.07	0.17	100
	0.00	90.66	9.13	0.04	0.18	100
	0.02	91.10	8.67	0.03	0.18	100
	0.00	90.92	8.91	0.04	0.13	100
Average:	0.00	90.99	8.75	0.09	0.17	100
Error:	0.01	0.39	0.40	0.05	0.02	

Table 1. Electron microprobe analyses of Fe-Si alloy starting materials containing 9 wt.% silicon. The corrected values have been scaled so that their totals equal 100%.

Electron Microprobe Analyses of 16 wt.% Silicon Starting Materials

Wt. %:	Al	Fe	Uncorrected			Total
			Si	Cr	Mn	
	0.09	82.70	15.47	0.29	0.97	99.51
	0.14	80.38	15.32	0.29	0.99	97.11
	0.07	82.86	15.64	0.30	0.91	99.78
	0.00	81.38	15.95	0.35	0.80	98.49
	0.10	79.96	15.43	0.33	0.75	96.58
Average:	0.08	81.46	15.56	0.31	0.88	98.29
			Corrected (Total = 100%)			
	0.09	83.11	15.54	0.29	0.97	100
	0.14	82.77	15.77	0.30	1.01	100
	0.07	83.04	15.67	0.30	0.91	100
	0.00	82.64	16.20	0.35	0.82	100
	0.11	82.80	15.98	0.34	0.78	100
Average:	0.08	82.87	15.83	0.32	0.90	100
Error:	0.05	0.20	0.26	0.03	0.10	

Table 2. Electron microprobe analyses of Fe-Si alloy starting materials containing 16 wt.% silicon. The corrected values have been scaled so that their totals equal 100%.

The sample itself is surrounded in the sample chamber by a pressure medium, which doubles as an insulator at high temperatures and sometimes a pressure calibrant for X-ray diffraction studies. Several pressure media are commonly used, including MgO, Al₂O₃, noble gasses and various halide salts. A primary criterion for a good pressure medium is its application of hydrostatic stress on the sample. Noble gasses such as Ar provide the most hydrostatic pressure (Dewaele et al., 2000), though they are considerably more difficult to load than solid materials. Spectroscopy-grade NaCl was used for some early experiments in this study. However, at low pressures the NaCl melted, obfuscating the optical signal. KBr was consequently used for subsequent experiments at the University of Maryland because of its high melting point at the

pressures in question (Boehler et al., 1996). NaCl was used for synchrotron studies because its equation of state is very well constrained (Decker, 1971; Fei, 2007) and it can therefore be used as a pressure calibrant.

Each sample is loaded as a three-layer sandwich of pressure medium, sample material and another layer of pressure medium. The pressure medium, after being desiccated in an oven, is flattened into a ~5-10 μm flake and placed at the bottom of the sample chamber. The sample material itself is also flattened and thinned as much as possible before it is loaded on top of this layer. By keeping the sample as thin as possible, the axial temperature gradient is reduced as well; early experiments showed that thin samples with limited topography are easiest to laser-heat as well. Finally, a layer of pressure medium is placed on top of the sample to ensure that the sample is not in contact with either diamond.

2.2. Optical Experiments

Optically-obtained melting curves are useful when XRD data are difficult to interpret. The technique has not previously been used on Fe-Si alloys, but it has been used effectively on wüstite (Fischer and Campbell, 2009) and platinum (Campbell, 2008).

2.2.1. Pressure Measurement

Small grains of synthetic ruby were also included in the sample chamber for use as a pressure calibrant. Pressure measurement using ruby was measured by shining a 532 nm laser on a ruby grain, which then fluoresced with a wavelength dependent on

the pressure as described by Mao et al. (1986). This wavelength was measured by a spectrograph. A pressure gradient of up to ~15 GPa has been measured across the radius of the sample chamber; even though the gradient is usually less than 5 GPa across the chamber, a ruby close to the center was always chosen to provide a consistent means of comparison between experiments. Thermal pressure due to expansion upon heating is not accounted for using this method. However, XRD experiments at APS indicate that thermal pressure is largely compensated by relaxation of the pressure medium; the resulting change in pressure is usually less than 2 GPa over a temperature range of over 2500 K (Table 3).

Thermal Pressure as a Result of Laser-Heating

Experiment	Adjusted Temp. (K)	d-Spacing (Å)	d-Spacing Error	Pressure (GPa)	Pressure Error (GPa)
Si9_103	300	2.8589	0.0476	61.5	12.3
Si9_104	1921	2.8835	0.0344	62.5	8.2
Si9_106	2318	2.8909	0.0028	62.5	0.9
Si9_110	2963	2.9016	0.0056	62.9	1.4

Table 3. Pressures calculated from a single sample’s NaCl pressure medium at various temperatures. The calculated pressures vary slightly because of a combination of thermal pressure and relaxation of the pressure medium. While the two variables do not cancel each other completely, the calculated pressures are well within error of each other. The large errors at low temperatures are due to the splitting of diffraction peaks caused by non-hydrostatic conditions within the diamond cell. As temperatures increased, the pressure became more hydrostatic and the peak splitting disappeared. The adjusted temperatures were calculated following the conclusions of Campbell et al. (2009), which indicate that the average temperature experienced by the pressure medium is 75% of the difference between the measured temperature and room temperature (300 K).

2.2.2. Laser-Heating and Temperature Measurement

The sample was heated by a 1064 nm fiber laser with a Gaussian distribution of intensity across the beam. In the experiments performed at UMD, the sample was heated on one side; because the data was obtained optically from the surface of the sample, any temperature gradient within the sample was irrelevant.

Laser heating results in a small area of the sample achieving high temperatures, and so the temperature of the heated spot must be measured optically. The light emitted from the heated spot was fed into a spectrograph; the resulting intensity-vs-wavelength curve was then fit to the Planck radiation function:

$$I = c_1 \cdot \varepsilon \cdot \lambda^{-5} / (\exp(c_2 / \lambda \cdot T) - 1) \quad (1)$$

In this equation, I is intensity, c_1 and c_2 are constants, ε is emissivity, λ is the wavelength, and T is temperature. A graph of $\ln(I \cdot \lambda^5)$ vs λ^{-1} was then constructed; this graph should be close to linear for temperatures under ~ 4000 K, so a linear fit indicates a good calibration. The temperature was then calculated from the slope of the curve, according to Wien's law, and the emissivity was calculated from its intercept at $\lambda^{-1} = 0$. Errors in temperature values are calculated from the curve's fit to the Planck function. This technique applies the greybody approximation, in which the emissivity is constant at all wavelengths but is not restricted to any particular value.

However, there are limitations to this approach. Because the laser beam has a Gaussian distribution, various parts of the laser-heated spot are at different temperatures simultaneously. By collecting all the light emitted from the spot, we can obtain an average temperature. By using a pinhole to restrict the area of the spot that is sampled, we can reduce the temperature gradient that is sampled and obtain a more

accurate peak temperature for the center of the spot. This follows procedures described by Heinz and Jeanloz (1987), Boehler et al. (1990) and Lazor et al. (1993).

However, Campbell (2008) demonstrated that there can be a significant and measurable gradient in temperature over the distance of only a few microns, and that study therefore introduced a new method to overcome this inaccuracy. In previous studies, the intensities of light emitted by the sample were observed at up to several hundred wavelengths. After some necessary calibration, these intensities were fit to Planck's Law and the temperature was derived from their slope. However, if the calibration is perfect, in theory only two points are needed to derive this slope. Campbell (2008) showed that by splitting the image of the laser-heated spot into four monochromatic wavelengths (650, 750, 800 and 900 nm) and by capturing the images on a two-dimensional CCD camera, a temperature map could be constructed for the sample in two dimensions. This method was used for the experiments at UMD, and the resolution of the CCD camera used is such that each pixel of the temperature map represents a $0.78 \mu\text{m}$ by $0.78 \mu\text{m}$ square on the sample (Figure 9).

Temperature Plot for Sample N38-4 (Fe-9Si, 21.8 GPa)

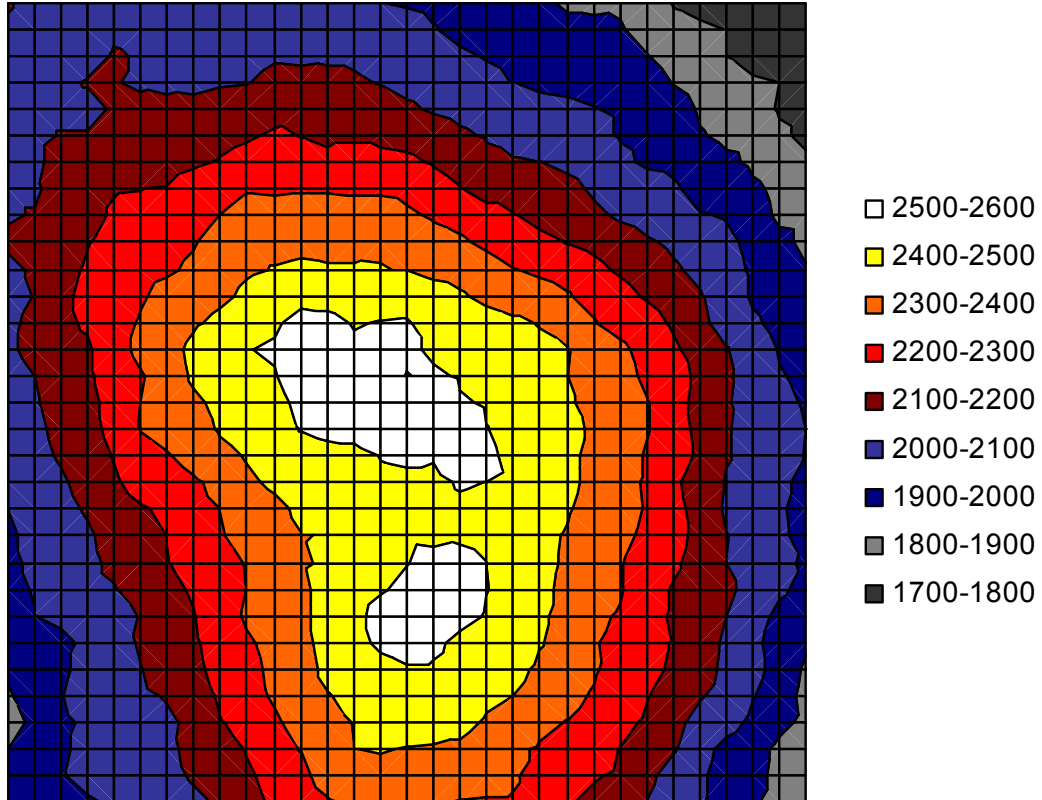
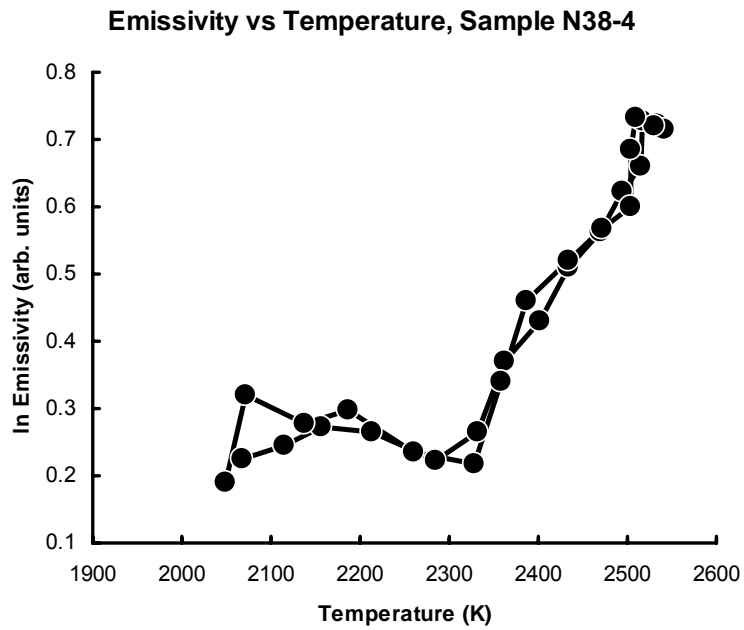


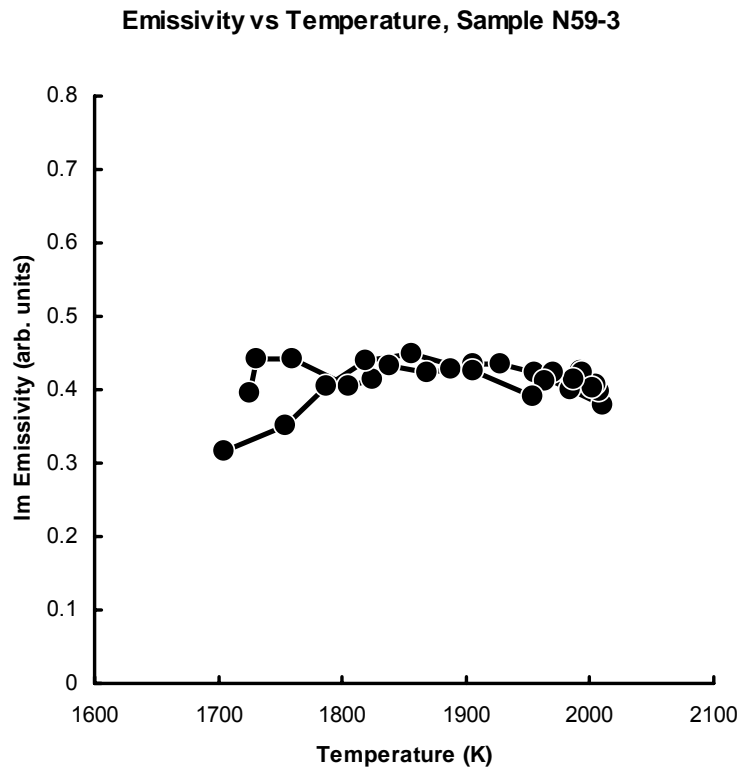
Figure 9. Two-dimensional temperature plot of sample N38-4; temperatures are in K. While laser-heated spots are treated in most studies as if they have a Gaussian temperature distribution, this plot shows that the temperature distribution has a complex topography, in this case with two peak hot spots. Each square is 0.78 μm on a side.

There are many advantages to having a two-dimensional temperature map of a laser-heated spot. Such spots are often idealized as circular for the sake of simplicity, but the true shape of the spot can clearly be demonstrated using this system. This is particularly helpful during analysis of recovered samples, for example by electron microprobe. If the temperature map can be correlated to a backscatter electron image of the sample, it is useful to know the temperature that was reached at a given location on the sample. Combined with the chemical composition at that location, important information about chemical diffusion and possibly phase stability can be obtained. Additionally, variations in the sample's amenability to heating can give insight into its topography or chemical homogeneity on the micron scale that is worth exploring further with the aid of an electron microscope.

When a material's emissivity and temperature are plotted against each other, a change in the trend can be seen when a change of phase occurs. By plotting these variables against each other, the temperature of a phase change can be determined. The simplest way to obtain this temperature is to plot a transect of pixels across the laser-heated spot (Figure 10). Ideally, the emissivity-temperature curve across one radius of the spot will exactly match the curve for the opposite radius. At a temperature where a kink or jump occurs in this curve, the sample has undergone a change of phase. As will be shown, this method has been used to produce melting curves for multiple compositions of Fe-Si alloys.



A)



B)

Figure 10. A) Plot of emissivity vs. temperature for a transect across sample N38-4. The kink in the curve at ~2330 K indicates the melting point. B) A similar plot for sample N59-3, showing no melting.

2.3. X-Ray Diffraction Experiments

Phase relations in the Fe-Si system are essential to determining whether silicon is a viable candidate for the Earth's core. Both sub-solidus phase stabilities and melting curves can be analyzed through X-ray diffraction studies, and these studies are greatly enhanced by the use of synchrotron radiation. Work was performed at beamline 13-ID-D, Advanced Photon Source at Argonne National Laboratory, a third-generation synchrotron source. The high available photon flux ensures that large amounts of data can be collected in relatively short periods of time. Experiments performed in March and July of 2008 produced more than of 1000 diffraction patterns at various pressures and temperatures. Patterns were selected for inclusion in phase diagrams primarily in order to encompass a wide variety of locations in P-T space; additional patterns were analyzed to clarify phase boundaries.

2.3.1. Pressure Measurement

Because the equation of state of NaCl is well constrained (Decker, 1971, Fei, 2007), it was used both as a pressure medium and a pressure calibrant – no ruby was required. Pressures were precisely calculated from these NaCl equations of state when presented in phase diagrams, tables and other figures in this study. One advantage of this approach is that thermal pressure can be calculated easily.

Pressures reported are based on NaCl lattice parameters while the samples were undergoing laser-heating. Unlike ruby fluorescence, this technique gives a precise value that does not require estimating the thermal pressure. These pressures were calculated using temperatures adjusted from those observed at the surface of the Fe-Si sample.

This follows the conclusion of Campbell et al. (2009) that the average temperature increase experienced by the pressure medium is 75% of the difference between the sample surface and room temperature. Thus, the adjusted temperatures were calculated using the equation:

$$T_{\text{NaCl}} = [(T_m - 300) \cdot 0.75] + 300 \quad (2)$$

In this equation T_{NaCl} is the adjusted temperature, T_m is the measured temperature at the surface of the sample, and room temperature is taken to be 300 K. This adjustment is necessary because the pressure medium experiences a sharp temperature gradient between the diamond, which is assumed to be at room temperature, and the laser-heated spot.

Changes to the X-ray diffraction pattern of NaCl can indicate changes in density due to changes in pressure. The density of the NaCl pressure medium was compared against its known equations of state to calculate the pressure at the spot where the X-ray beam was focused. NaCl takes two structures: the B1 structure up to ~28 GPa, and the B2 structure above that pressure. Data used for pressure calculations came from Decker (1971) (B1) and Fei et al. (1997) (B2). Those studies provided one-bar volumes, bulk moduli and the pressure derivatives of the bulk moduli when fit to the third-order Birch-Murnaghan equation:

$$P = \frac{3}{2} \cdot K_0 \cdot (x^{7/3} - x^{5/3}) \cdot [1 + \frac{3}{4} \cdot (\frac{\delta K}{\delta P} - 4) \cdot (x^{2/3} - 1)] \quad (3)$$

In this equation, P is pressure, K_0 is the bulk modulus, and x is ρ/ρ_0 (the ratio of a material's density under pressure to its density at one bar).

2.3.2. Laser-Heating and Temperature Measurement

Samples at APS were laser-heated using the same type of laser as at UMD, but using two lasers to heat both sides of the sample. By heating from both sides, the axial temperature gradient was minimized. This is important when considering the composition and structure of the phases in the interior of the sample (i.e. in XRD experiments).

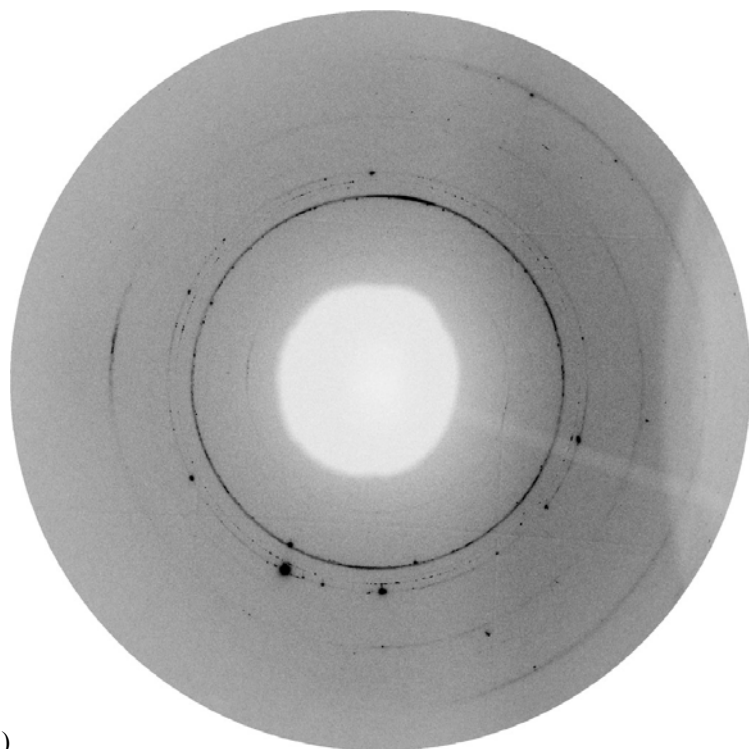
Temperatures at the APS synchrotron were calculated from the Planck radiation function (Equation 1), averaging the temperature over the central 5 μm of the laser-heated spot (Shen et al., 2001). This method was described in detail by described by Heinz and Jeanloz (1987), Boehler et al. (1990) and Lazor et al. (1993). The lasers and temperature measurement system were aligned with the x-ray beam, allowing temperatures to be correlated with x-ray diffraction patterns. The laser-heating system at APS was described in detail by Shen et al. (2001, 2005) and Prakapenka et al. (2008).

2.3.3. Analysis of X-Ray Diffraction Patterns

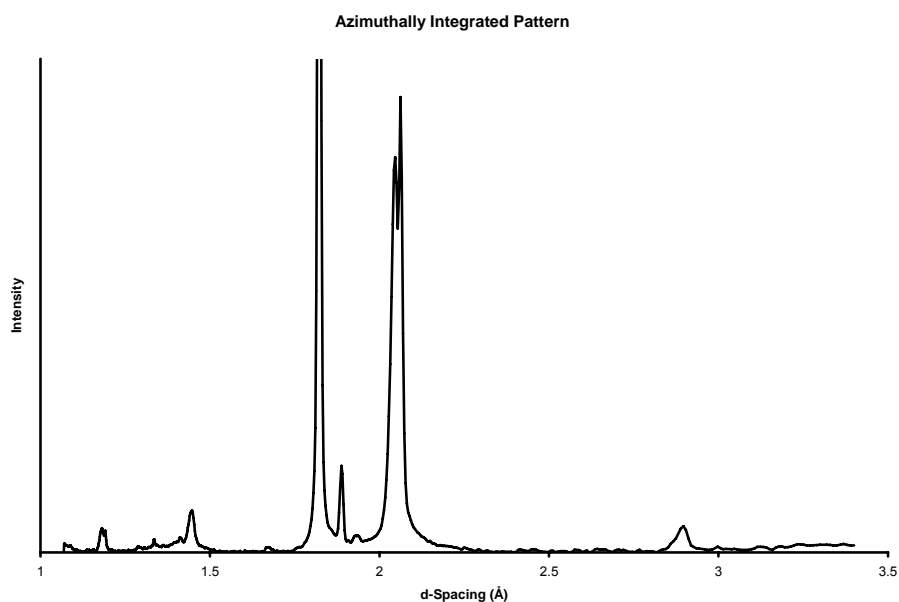
X-ray diffraction patterns were collected using a 2-dimensional CCD detector; this method collects a pattern of rings of diffracted X-rays of various diameters (Figure 11). These patterns are integrated azimuthally using Fit2D software (Hammersley et al., 1996) to better illustrate the relationship between the diffraction rings and their angle to the main X-ray beam. Each ring appears as a peak on such a plot; the relationship between the peak's angle to the main X-ray beam and the crystal structure of the sample is given by the Bragg Diffraction Equation:

$$\lambda = 2 \cdot d \cdot \sin(\theta) \quad (4)$$

In this equation, λ is the wavelength of the photons (0.3344 Å was used), θ is the angle of X-ray diffraction relative to the incident X-ray beam, and d is a measure of the distance between planes in an idealized crystal lattice. The parameters of the unit cell can be calculated from these d -spacings, giving important physical information such as the crystallographic structure and the density of the material.



A)



B)

Figure 11. A) Two-dimensional x-ray diffraction pattern for sample Si9_104 (Fe-9Si, 59.1±3.1 GPa, 2461 K). The center of the detector is blocked to prevent the x-rays from damaging it, and the linear shadow on the right side is the arm holding the beam blocker. Other equipment shadows can be seen partially blocking the x-rays on the right side of the pattern. **B)** The azimuthal integration of the same pattern. The top of the tallest peak has been chopped off here to make the smaller peaks more visible.

3. Results

Melting curves for both compositions of starting material were constructed from the data obtained at UMD. Phase diagrams for both compositions were constructed from XRD data. Calculations were made based on the XRD data that show iron and silicon atoms compress similarly up to at least 90 GPa.

3.1. Optically Determined Melting Curves

A melting curve has been constructed for two compositions of Fe-Si alloy, 16 wt% silicon (henceforth Fe-16Si) and 9 wt% silicon (Fe-9Si). The melting curves extend up to 52 GPa (Figure 12, Table 4). This data was collected using the two-dimensional temperature mapping system described by Campbell (2008) and the temperature-emissivity relationships previously described (Figure 10).

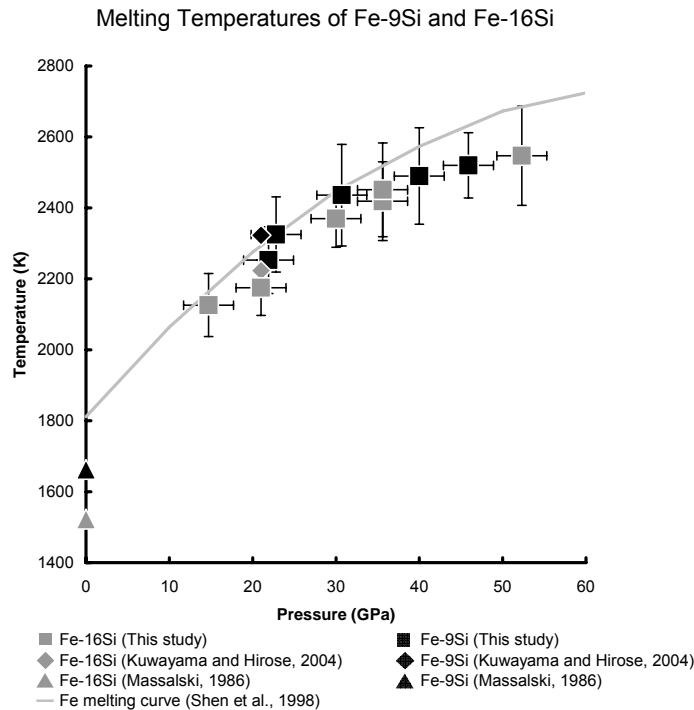


Figure 12. Melting temperatures for Fe-9Si and Fe-16Si obtained using the method of Campbell (2008).

Melting Temperatures of Iron-Silicon Alloys

Wt.% Si	Pressure (GPa)	Temperature (K)	Temp. Error
9	0	1663*	
9	21	2323**	
9	21.9	2253	94
9	22.8	2325	106
9	30.7	2436	143
9	40.0	2490	136
9	45.9	2520	92
16	0	1523*	
16	14.7	2126	89
16	21.0	2175	78
16	21	2223**	
16	30.0	2370	81
16	35.6	2419	111
16	35.6	2451	132
16	52.3	2547	140

Table 4. Melting temperatures obtained using the method of Campbell (2008). *From Massalski (1986);

**From Kuwayama and Hirose (2004). Errors are ± 2 GPa and ± 150 K for new data.

Where pressure was measured by ruby fluorescence, error was estimated to be ± 3 GPa for all samples. This value is based on an average pressure gradient across the sample chamber of about 5 GPa, which has been obtained by fluorescing rubies at the centers and rims of various sample chambers. Because the rubies measured were very close to the samples being heated, it is estimated that the pressure difference between the ruby and the laser-heated spot was no more than 2 GPa. It has been suggested that relaxation of the pressure medium with heating roughly compensates for thermal pressure (Heinz and Jeanloz, 1987); Dewaele et al. (2007) showed that, for soft pressure media, a pressure measurement taken at room temperature is accurate to within about 3 GPa at high temperatures as well. Thus, the estimated error for ruby fluorescence measurements is 3 GPa, taking into account thermal pressure and the

pressure gradient within the sample chamber. Error in temperature measurements is shown as the error in fitting the curve of $\ln(I \cdot \lambda^5)$ vs λ^{-1} to the Planck function.

The curves obtained in this study are interpreted to be solidi because the optical properties are expected to be larger across the solidi than the liquidi. This interpretation assumes that there is a greater change in optical properties across a solid-liquid transition than a solid-solid transition. The curves match closely the results of Kuwayama and Hirose (2004) and are in agreement with 1 bar data from Massalski (1986). When compared to the pure iron melting curve of Shen et al. (1998), Fe-9Si has a melting point depression of ~ 50 K at 21 GPa, and Fe-16Si has a melting point depression of ~ 150 K at that pressure. Both these depressions increase with increasing pressure above approximately 30 GPa (Figure 12), and the curves intersect at approximately 50 GPa and 2500 K. The same technique was attempted for determining the melting curve of pure iron, but no discontinuity in the temperature vs. emissivity trend was observed. As a result, no melting temperatures were obtained, perhaps because of a small difference in emissivity between solid and liquid iron.

3.2. X-ray Diffraction Results

Data on melting and sub-solidus phases have been obtained using X-ray diffraction techniques at the APS synchrotron. (An example of an azimuthally integrated XRD pattern is shown in Figure 13). These data have been analyzed to determine the phases present at a given composition, temperature and pressure. A complete record of all XRD data is included in the Appendix.

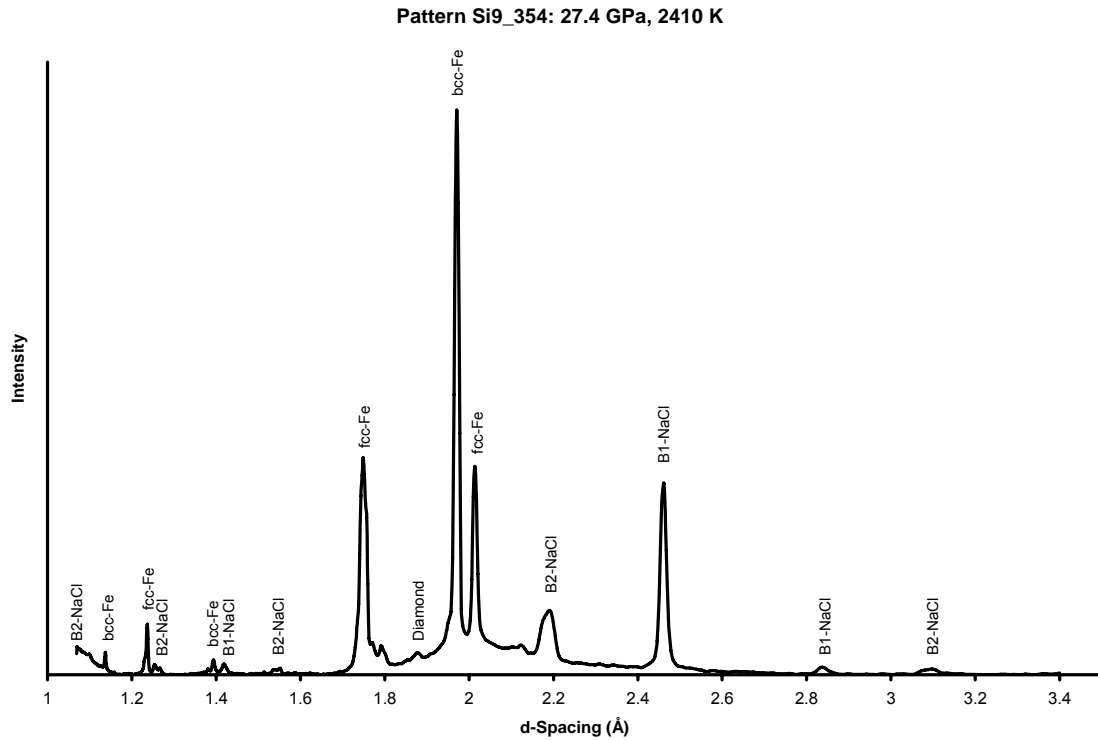


Figure 13. An azimuthally integrated XRD pattern for Fe-9Si at 27.4 GPa and 2410 K. The B1-NaCl and B2-NaCl peaks indicate the low and high pressure phases (respectively) of the sodium chloride pressure medium. Both structures are sampled by the X-ray beam because of the large temperature gradient between the diamonds and the sample. Although diamond peaks are usually not seen because carbon is an extremely weak refractor of X-rays, this pattern does show a small diamond peak. The apparent high background around 2Å is a small band of melt scattering. The other structures shown are discussed in the text.

A sample of pure iron was also studied during the synchrotron experiments as a test of the repeatability of conditions at the beamline facility. Data were collected to find the temperature of the HCP-FCC transition at 40 GPa. This value is already well known from several sources including Shen et al. (1998), who used the laser-heating system at this beamline (APS 13-ID-D) to measure the phase diagram of iron. The results obtained from this pure iron sample (Figure 14, Table 5) are within error of the results of Shen et al. (1998), which suggests that accurate temperatures were recorded at the beamline. Phase transitions for pure iron, as well as Fe-Si alloys, were plotted at the lowest temperatures at which the higher-temperature phase was observed.

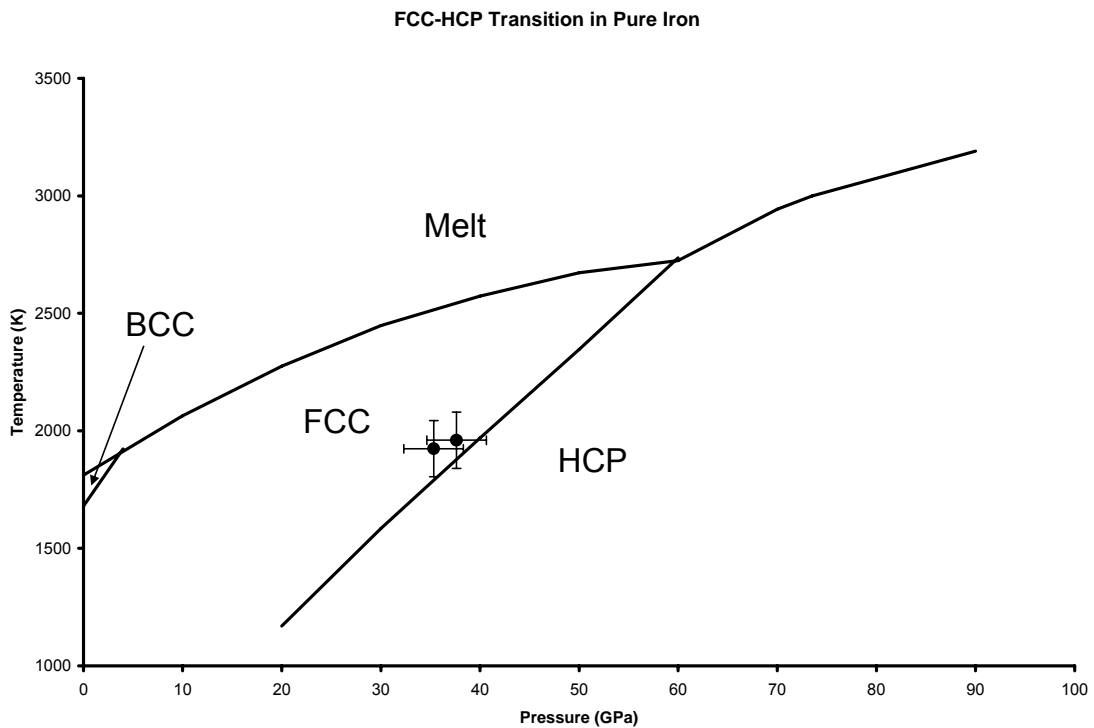


Figure 14. Results of an experiment to determine the temperature of the HCP-FCC transition in pure iron at approximately 40 GPa. The phase diagram is from Shen et al. (1998). The temperatures measured are slightly higher than previously published values, but they are within error of the transition from Shen et al. (1998).

Measured Pressures and Temperatures for the HCP-FCC Transition

Pressure (± 3 GPa)	Temperature (± 120 K)
37.6	1960
35.3	1924

Table 5. Two points measured on the HCP-FCC transition in pure iron. The temperatures reported are the lowest temperatures at which FCC was seen.

Pressure-temperature-phase data have been compiled from XRD data for the two compositions of starting material (Table 6). The stability fields of HCP and FCC for Fe-9Si (Figure 15) are similar to those by Lin et al. (2002, 2009) except that the temperatures for the new data are significantly higher. Lin (2002) showed the BCC structure to appear above ~ 1600 K at 60 GPa; the new data show it to appear above ~ 2700 K at that pressure. The stability field of the BCC phase is extended to high pressures and temperatures, where it coexists with FCC and HCP. However, this study's data shows a transition from BCC to the B2 structure at about 40-50 GPa. The B2 structure is a higher ordering of the BCC structure (Figure 16); consequently, the change in volume across the transition is only $0.9 \pm 0.1\%$ and the diffraction patterns appear similar, if not entirely identical. The B2 phase was identified by the presence of peaks in which the sum of the values of h, k and l in the plane (hkl) is an odd number. This peak was usually (100) or (210); the BCC phase only has peaks in which the sum of h, k and l is even. The transition has Clapeyron slope of -45 ± 3 K/GPa. This value was obtained by linear regression of the five data points closest to the transition.

Phases Determined in XRD Analyses

Wt.% Si	Pressure (GPa)	Temp. (K)	Phase(s)	Wt.% Si	Pressure (GPa)	Temp. (K)	Phase(s)
9	20.3 (0.7)	1541	FCC+BCC	16	21.1 (1.6)	2012	BCC
9	20.4 (0.8)	1646	FCC+BCC	16	21.7 (1.2)	2280	BCC
9	10.3 (1.3)	1786	FCC+BCC	16	21.5 (1.2)	2463	BCC
9	18.7 (0.9)	2053	FCC+BCC	16	22.2 (1.5)	2700	Melt
9	22.3 (1.2)	2006	FCC+BCC	16	22.3 (1.2)	2887	Melt
9	27.4 (1.8)	2410	FCC+BCC	16	25.0 (1.4)	2501	BCC
9	28.0 (1.4)	2263	FCC+BCC	16	29.1 (2.0)	2685	Melt
9	28.2 (2.3)	2688	FCC+BCC	16	28.6 (1.4)	2142	HCP
9	28.0 (2.7)	2947	FCC+BCC	16	47.3 (1.5)	2188	HCP
9	29.3 (1.2)	3048	FCC+BCC	16	47.2 (1.7)	2507	HCP
9	25.6 (3.4)	2000	HCP+BCC	16	49.2 (2.3)	2619	B2
9	32.2 (2.1)	2078	FCC+BCC	16	50.3 (1.5)	2872	Melt
9	44.3 (1.6)	2183	HCP+BCC	16	50.0 (1.7)	2715	Melt
9	44.8 (1.4)	2411	HCP+BCC	16	52.1 (1.7)	2121	B2+X
9	45.2 (1.4)	2494	HCP+BCC	16	52.3 (1.8)	2410	B2+X
9	46.3 (1.9)	3179	FCC+B2	16	52.0 (1.9)	2497	B2+X
9	47.9 (1.5)	3374	FCC+B2	16	58.0 (1.4)	2862	Melt
9	45.6 (1.6)	2307	HCP+BCC	16	57.9 (1.8)	2987	Melt
9	46.2 (1.8)	3053	FCC+B2	16	65.0 (1.7)	1756	B2+X
9	52.2 (1.6)	2678	HCP+BCC	16	65.6 (1.5)	2012	B2+X
9	51.9 (1.4)	2500	HCP+BCC	16	66.2 (1.5)	2157	B2+X
9	52.0 (3.1)	2982	HCP+B2	16	66.8 (1.5)	2326	B2+X
9	61.7 (1.5)	2880	HCP+B2	16	66.9 (1.5)	2499	B2+X
9	62.5 (1.5)	2991	HCP+B2	16	68.1 (1.9)	2850	B2+X
9	59.1 (3.1)	2461	HCP+B2	16	67.8 (1.9)	3036	Melt
9	61.5 (2.8)	3340	HCP+B2	16	68.0 (1.7)	3130	Melt
9	62.6 (1.8)	3487	HCP+B2	16	74.0 (1.9)	2143	B2+X
9	62.9 (1.8)	3851	HCP+B2	16	76.0 (1.8)	2790	B2+X
9	67.2 (5.5)	2066	HCP	16	76.0 (1.5)	3038	Melt
9	69.0 (2.2)	2654	HCP	16	76.0 (2.0)	3105	Melt
9	70.6 (2.5)	2729	HCP+B2	16	88.1 (1.8)	2063	B2
9	70.3 (1.4)	2760	HCP+B2	16	89.6 (1.5)	2500	B2
9	70.9 (1.5)	3006	HCP+B2	16	89.5 (1.7)	2883	B2
9	70.8 (3.3)	3091	HCP+B2	16	91.6 (2.0)	3105	B2
9	78.5 (1.8)	2254	HCP				
9	79.6 (1.6)	2457	HCP				

Table 6. Phases observed in Fe-Si alloys in X-ray diffraction patterns. The various phases are discussed in the text. Uncertainties in pressure are given in parentheses. Temperature measurements are accurate within ± 120 K.

Phase Diagram of Alloy with 9 wt% Si

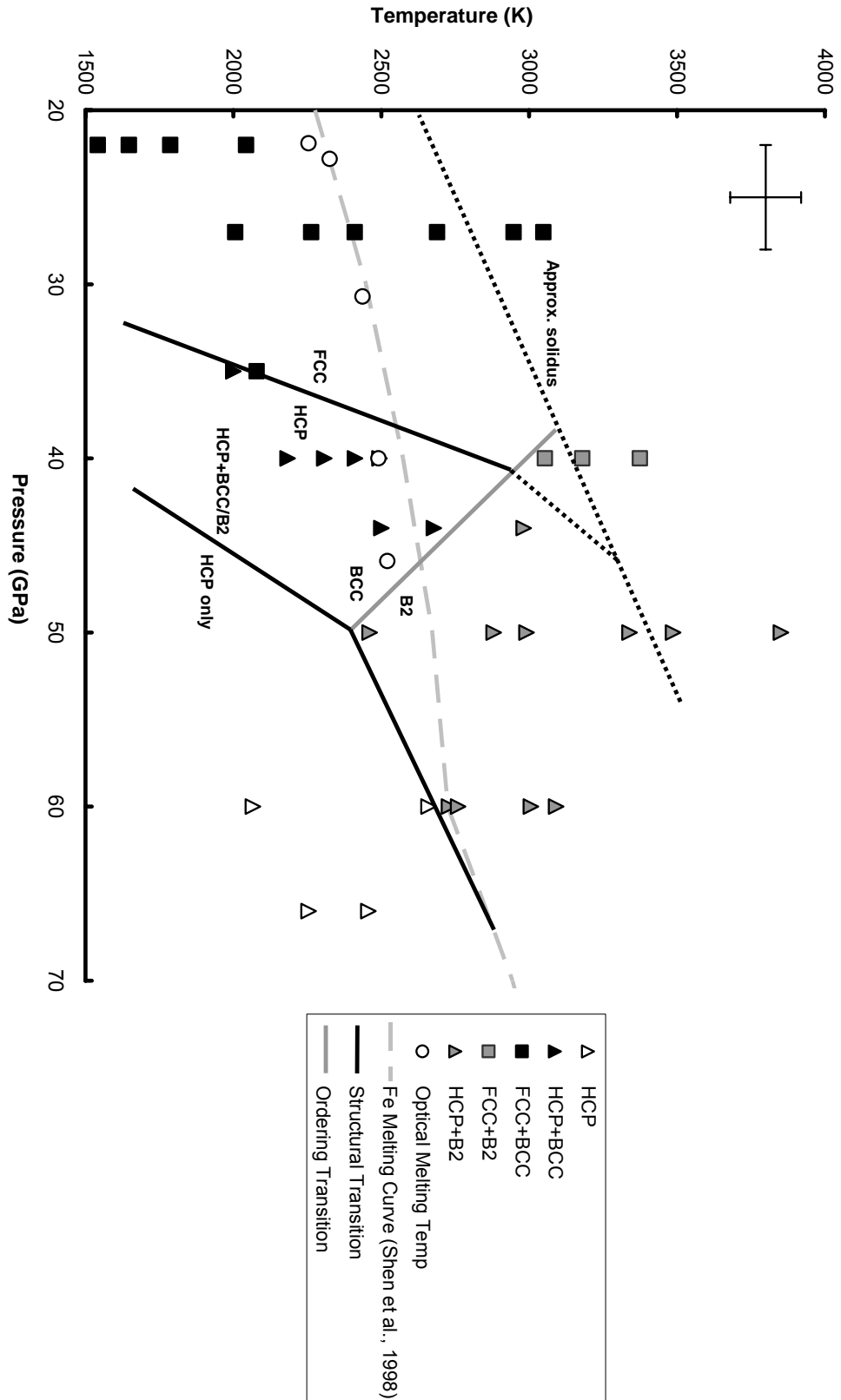


Figure 15. Phase diagram for Fe-9Si. Estimated transitions are dotted.

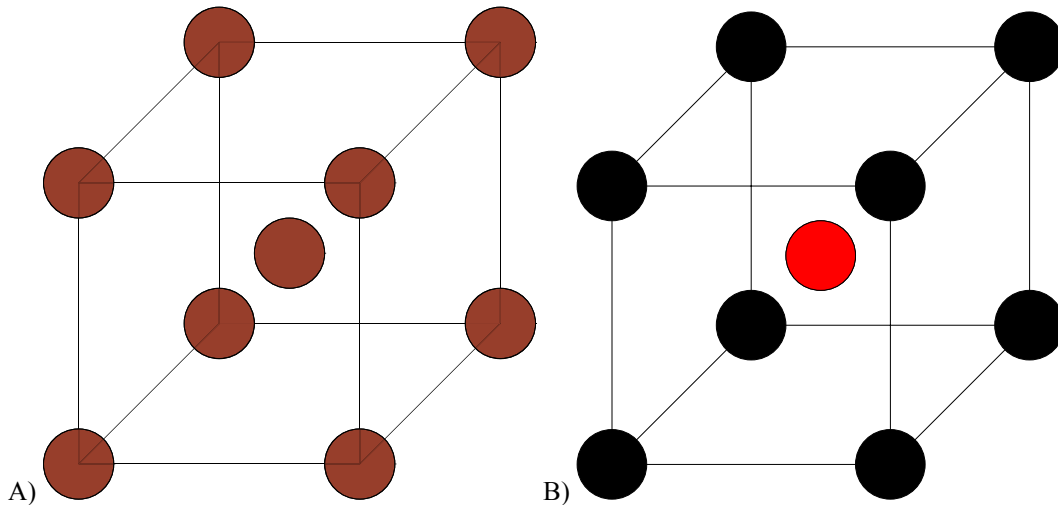


Figure 16. Demonstration of ordering between the BCC and B2 structures. **A)** The BCC structure, with the silicon and iron atoms randomly distributed among all the sites in the unit cell. **B)** The B2 structure has the same layout of atoms, the site in red preferentially contains silicon over iron. The silicon and iron atoms are not identically effective at scattering X-rays, so when they are ordered like this, constructive interference creates new, odd-numbered peaks such as (100), (111) and (210).

In Figure 15, solid phases appear in diffraction patterns well above the pure-Fe melting curve of Shen et al. (1998). This contradicts the optically obtained melting curve for this composition, which is lower than that of pure iron. The approximate solidus is marked where I observed a strong melt diffraction scattering pattern coexisting with solid phases (Figure 17).

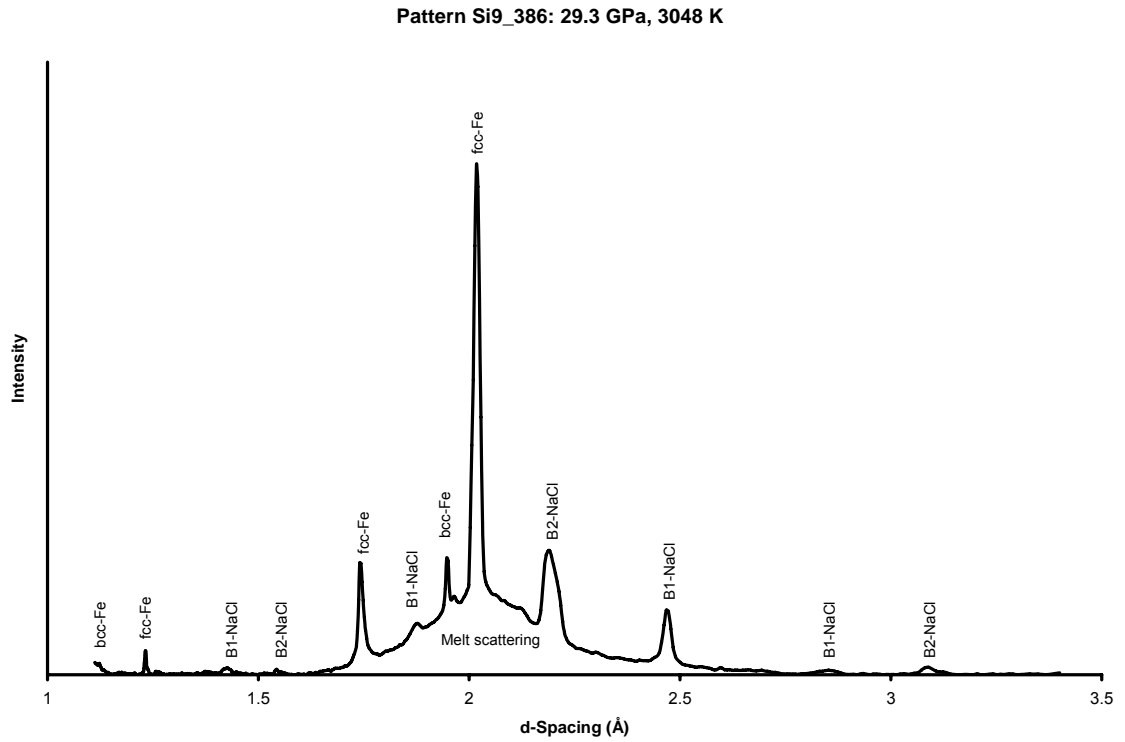


Figure 17. An azimuthally integrated XRD pattern for Fe-9Si at 29.3 GPa and 3048 K. Peaks for BCC-Fe and FCC-Fe, as well as the NaCl pressure medium, can be seen. The wide, indistinct band centered around 2Å is the result of melt scattering, and so this data point is shown above the approximate solidus in Figure 15.

The phase diagram for Fe-16Si (Figure 18) is different from that of Fe-9Si, and it is more obvious in the XRD pattern when melt is the dominant phase. The BCC and HCP structures are observed at low pressures, and between 45 GPa and 70 GPa there is a two-phase field comprised of B2 and an unidentified phase. This phase appears to be of orthorhombic or lower symmetry, and it produced much weaker diffraction peaks than NaCl or metal B2 in the same samples (Figure 19). This phase will be referred to henceforth as Phase X; a list of d-spacings for Phase X is shown in Table 7. At 82 GPa the alloy takes only the B2 structure. The melting temperature is above the pure-Fe melting curve from Shen et al. (1998), but not as high as the approximate solidus of Fe-9Si.

Phase Diagram of Alloy with 16 wt% Si

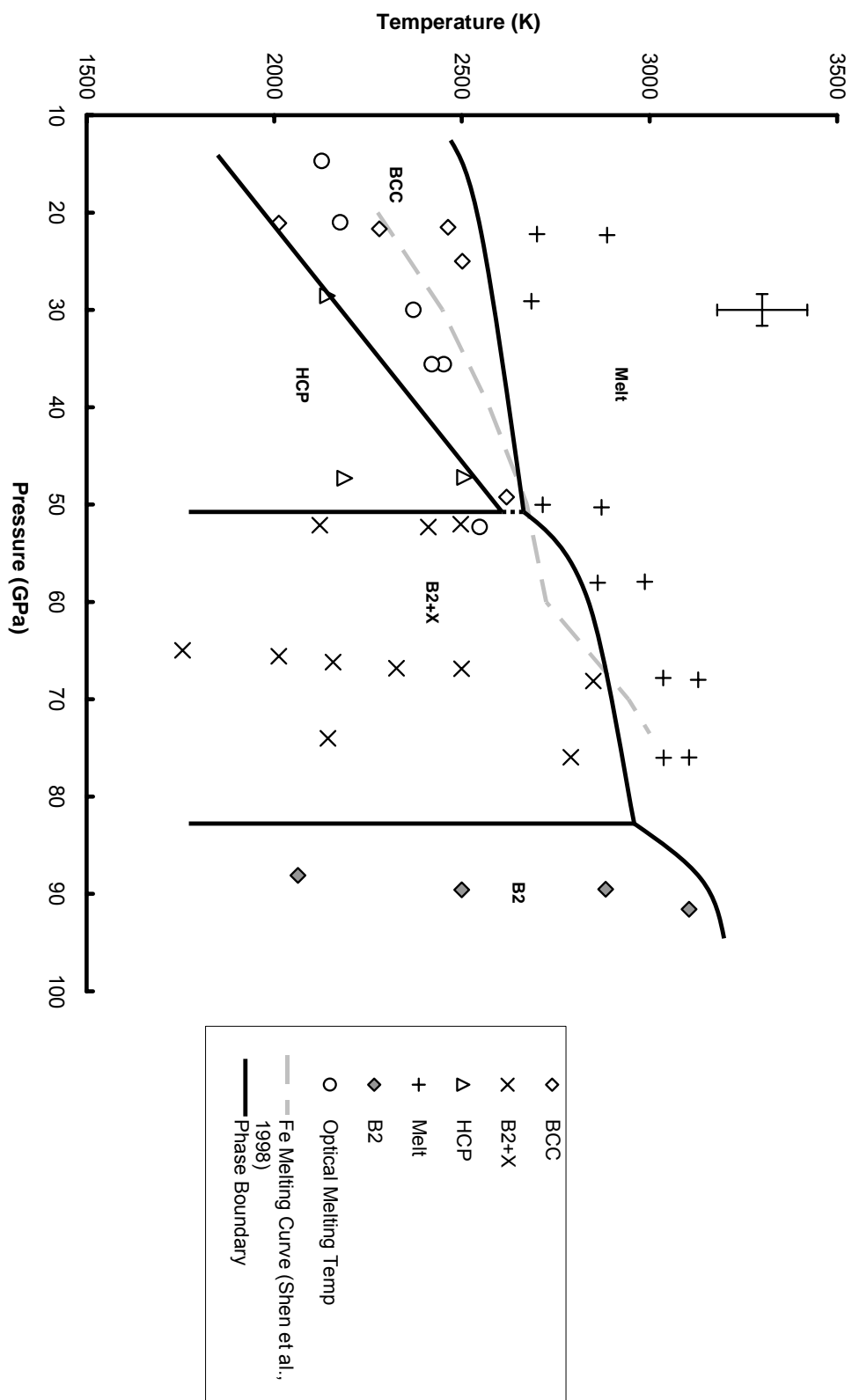


Figure 18. Phase diagram for Fe-16Si. Estimated transitions are dotted.

Pattern Si16_012: 66.8 GPa, 2843 K

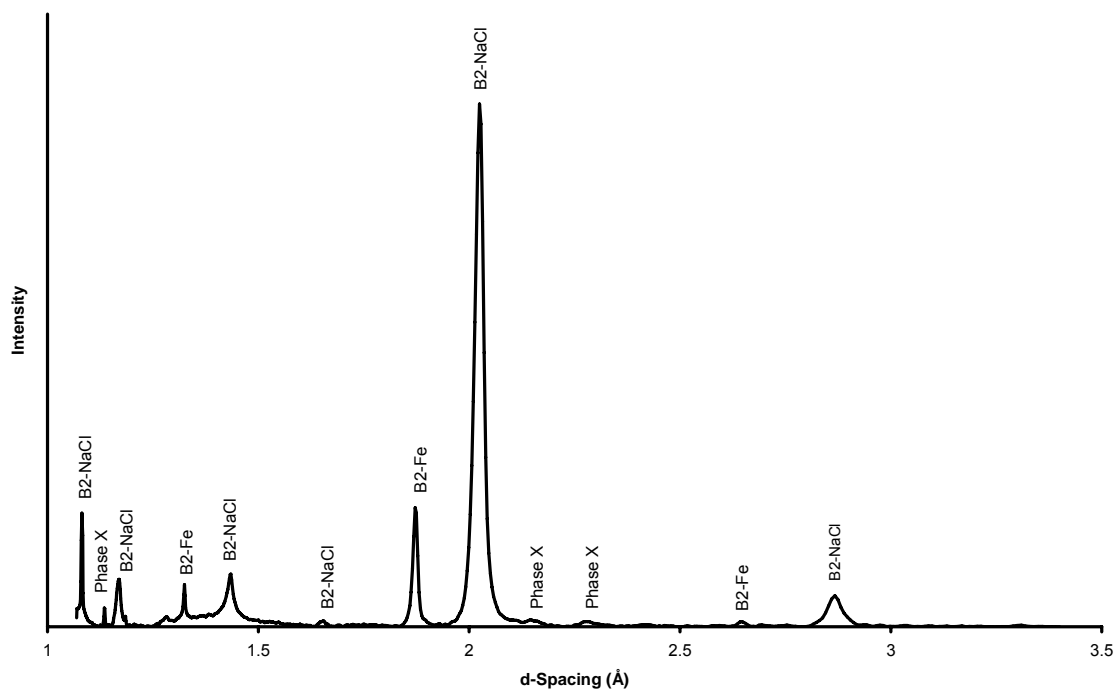


Figure 19. An azimuthally integrated XRD pattern for Fe-16Si at 66.8 GPa and 2843 K. At this temperature and pressure, the alloy takes on the B2 structure and a coexisting phase of orthorhombic or lower symmetry, labeled here as Phase X.

d-Spacings of Phase X

	Si16_012	Si16_016	Si16_036	Si16_038	Phase	HKL
Pressure (GPa):	66.81	68.13	74.02	75.96		
Temperature (K):	2326	2850	2143	2790		
	2.867	2.872	2.841	2.841	NaCl	(100)
	2.645	2.661	2.631		B2	(100)
		2.423			X	
	2.281	2.288	2.277	2.282	X	
	2.146	2.139			X	
			2.042		X	
	2.024	2.027	2.001	2.004	NaCl	(110)
			1.912	1.939	X	
	1.872	1.871	1.859	1.863	B2	(110)
				1.670	X	
	1.652	1.651	1.636	1.635	NaCl	(111)
	1.433	1.435	1.419	1.420	NaCl	(200)
	1.325	1.326	1.315	1.316	B2	(200)
	1.282		1.269	1.271	NaCl	(210)
	1.180				B2	(210)
	1.168	1.168	1.156	1.157	NaCl	(211)
	1.135				X	
	1.082			1.074	B2	(211)

Table 7. List of d-spacings for patterns showing B2 and Phase X. In the Phase column, NaCl is the B2-NaCl structure, B2 is the B2-Fe-16Si structure and X is Phase X.

3.3. Calculations of Atomic Density

Atomic volumes were calculated for all phases, although where B2 coexists with Phase X, only the volume of B2 was calculated because the structure of Phase X remains unsolved. The density of pure iron was also calculated at the same pressures and temperatures from the equation of state of Dewaele et al. (2006) (Figure 20). This equation of state was used because it incorporates data from several sources. It incorporates experimental data from diamond anvil cell studies using helium as a pressure medium, which provides quasihydrostatic conditions above 100 GPa (Dewaele et al., 2004). The study also considers shock wave data and theoretical evaluations of heat capacity.

The temperatures used in the calculations were reduced by 7% from those recorded during the experiments to account for the calculated axial temperature gradient within the samples. The magnitude of the reduction was calculated using the techniques of Campbell et al., 2007. Atomic volume ratios of the Fe-Si alloys to pure iron did not change with pressure and were within $\pm 1\sigma$ of 1.0 (Figure 21). This trend indicates that iron and silicon atoms occupy the same volume and are compressed by an identical percentage at any given pressure.

There is some scatter in the data, especially from the BCC phase. There is more scatter for Fe-9Si than Fe-16Si due to the common presence of two coexisting phases. The largest uncertainties are due to split diffraction peaks in BCC and B2 patterns, which occur frequently at low temperatures. If the temperature measurements for either composition are inaccurate, the calculated densities of iron at identical conditions would be inaccurate as well. This could account for the scatter in Figure 21.

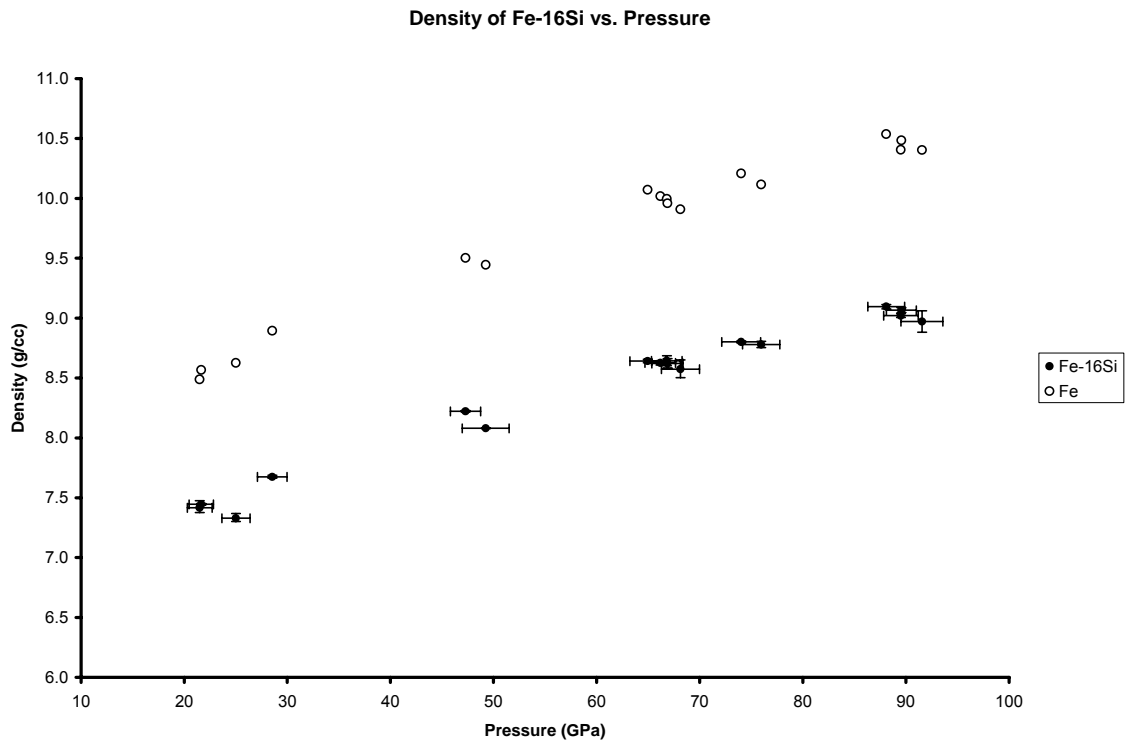


Figure 20. Plot of density of Fe-16Si and pure iron against pressure. Phase X was not included in this plot, but nevertheless the trend is linear, suggesting that Phase X is of very small abundance and can be ignored in density calculations for the alloy. Densities of iron were calculated from the equation of state of Dewaele et al., 2007. The apparent scatter in the data exists because calculations were made at a wide range of temperatures.

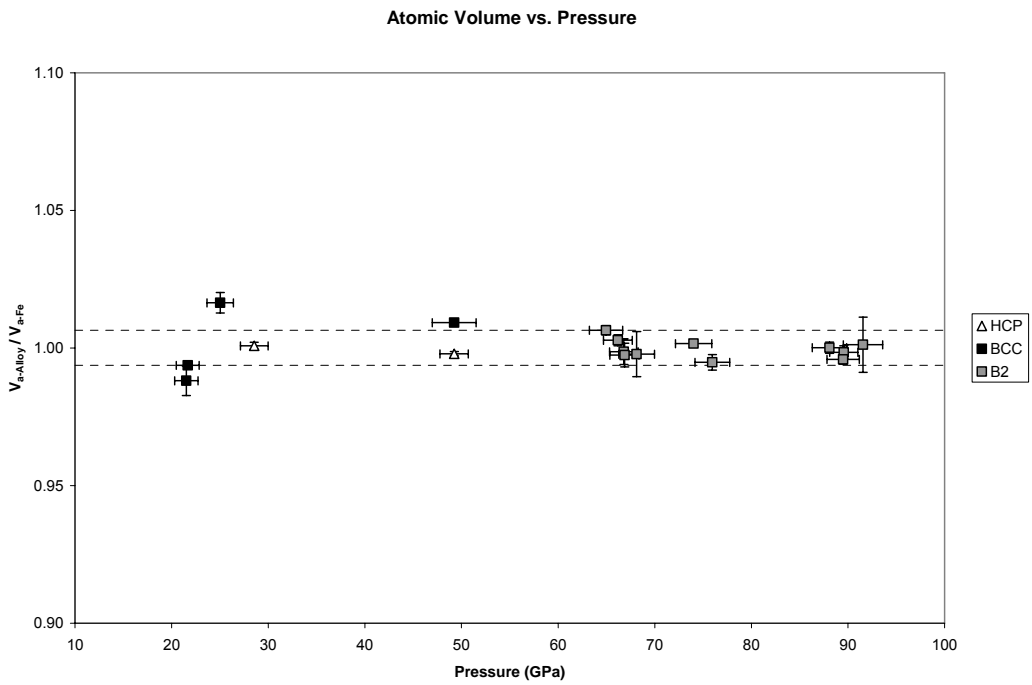
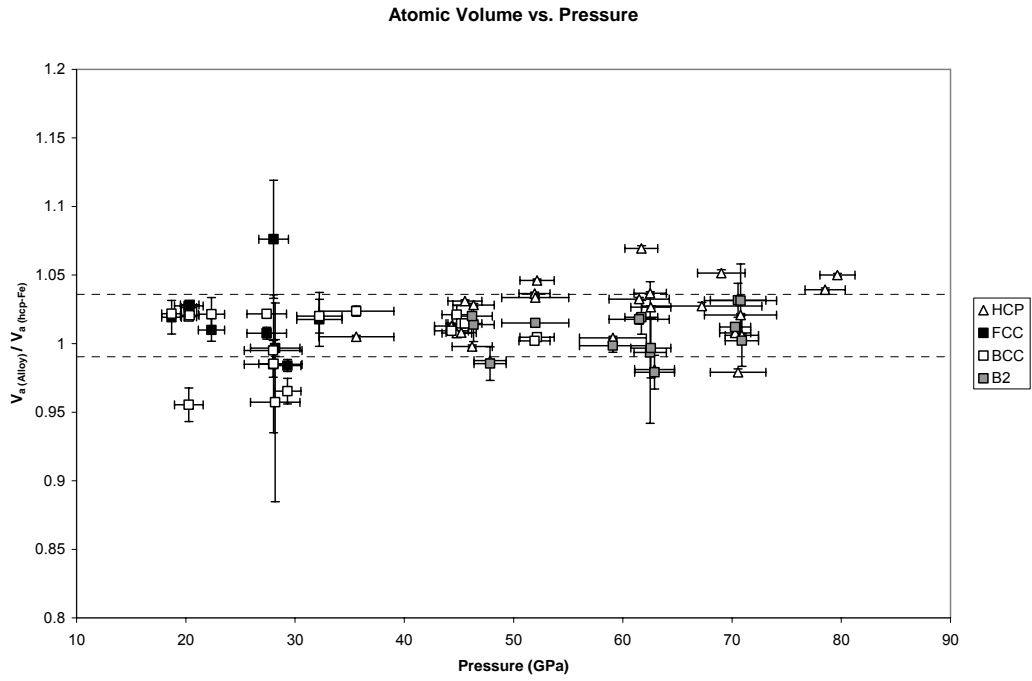


Figure 21. Comparison of atomic volumes of **A)** Fe-9Si and **B)** Fe-16Si to the atomic volume of pure iron at identical conditions. Structural transitions do not influence the volume ratios. Dashed lines show 1σ bounds.

4. Discussion

The experiments previously described are designed to gain a better understanding of the Earth's core, particularly its composition and physical properties. Phase diagrams are essential to the extrapolation of physical properties to high pressures. Equations of state cannot extrapolate across phase transitions, so all of a material's phases must be known before its density at high pressure can be estimated. The melting curve must also be described if the thermal structure and cooling rate of the core are to be understood.

4.1. Optical Melting Curves

The optical melting curves are in agreement with data from Kuwayama and Hirose (2004). While the curves were not extended to atmospheric pressure, it appears likely that they are also in agreement with data from Massalski (1986). Consequently, the method described by Campbell (2008) appears to accurately reproduce published melting temperatures in diamond anvil cell samples.

The melting curves of Fe-9Si and Fe-16Si appear to intersect at approximately 50 GPa and 2500 K (Figure 12). This is near a triple-point for both compositions (Figures 15 and 18), though the temperatures are uncertain based on XRD data, as will be discussed. The B2 structure exists above this pressure in both compositions, but it is unclear whether the presence of B2 unifies the melting curves. Measuring melting temperatures at higher pressures should clarify whether the two melting curves follow the same trajectory or if they cross.

Fischer and Campbell (2009) used the same techniques to measure melting and sub-solidus phase transition temperatures in wüstite ($\text{Fe}_{0.94}\text{O}$), but no sub-solidus information has been obtained for Fe-Si alloys using this method. It appears that the optical transitions of certain materials are better suited than others to the method of Campbell (2008). Experiments for this study were more consistently successful on samples of Fe-16Si than Fe-9Si. There were numerous experiments for both compositions that did not yield conclusive melting temperatures, but it appears that samples containing more silicon are easier to study optically. This is borne out by numerous attempts to measure the melting temperature of pure iron, all of which were unsuccessful. It is possible that a different pressure medium will help to clarify the optical signal and thus produce more consistent results.

4.2. The Fe-9Si and Fe-16Si Phase Diagrams

There are dramatic differences between the phase diagrams for the two compositions studied. The Fe-9Si diagram is an adjustment of the pure iron phase diagram that shows the BCC/B2 structure stabilized to high pressures at high temperatures. This stabilization has been calculated (Belonoshko et al., 2003) and observed in other studies (Lin et al., 2002, 2009; Asanuma et al., 2008).

The diagram for Fe-16Si is notable for several features. There is no FCC present, but a field containing a combination of B2 and Phase X. The weak diffraction peaks of Phase X (Figure 19) suggest that it is modally sparse compared to the coexisting B2. Therefore, the lever rule requires that the composition of the B2 phase be not far from the starting composition of the sample, 16 wt.% Si. A plot of density vs.

pressure where B2 is considered to be the only phase present (Figure 20) supports this because it shows a consistent, linear trend at all pressures.

The calculations of Brosh et al. (2009) for a composition with 8 wt.% silicon do not agree with the data obtained in this study. Brosh et al. (2009) show a field of HCP+BCC below ~40 GPa and above ~1500 K (Figure 7), which experiments show is dominated by a field of FCC+BCC. Brosh et al. (2009) also predict the stabilization of FCC to ~80 GPa and ~2500 K, which was not observed in experiments. The B2 phase was not predicted at all for this composition, even though Brosh et al. (2009) predicted a B2+HCP field for a composition with 4 wt.% silicon.

4.3. XRD Melting Data

For Fe-9Si, every phase (BCC, B2, HCP and FCC) was observed coexisting with melt under some pressure-temperature range (Figure 15). In three different two-phase fields (FCC+BCC, FCC+B2 and HCP+BCC), both phases' diffraction peaks grew smaller with increasing temperature above the estimated solidus. In some diffraction patterns, only the (200) peak could be identified for the BCC or B2 phase, but that peak was strong enough to indicate the presence of some solid with those structures. The simultaneous weakening of both solid phases' diffraction peaks suggests that a separate liquidus and solidus exist close to one another in temperature, and the field between them was missed in the experiments. This is supported by the closeness of the melting curves of iron and Fe-Si alloys (Figure 12).

According to the XRD data, solid phases continue to exist at temperatures far above the optical melting curve. Measurement of the FCC-HCP transition in pure iron

(Figure 14) using the same methods indicates that the temperature measurement system at the synchrotron beamline was recording accurate temperatures. It is unlikely that the laser and x-ray beams went out of alignment as the temperature increased, and they were re-aligned every time the sample was removed and replaced into position. Thermal expansion of the diamond cell has been observed to defocus the laser beams, but it has not been obviously responsible for moving the beam off target. Diamonds are sufficiently transparent to X-rays that moving the anvils during heating should have no effect on the X-ray beam.

Therefore, the most reasonable explanation is that a high axial temperature gradient existed across the samples' interiors. Such a gradient has been suggested in previous studies (e.g. Lin et al., 2002) and has been modeled by Campbell et al. (2007). While the temperature is measured radiometrically from the surface of the sample, the interior of the sample may be sufficiently cooler to exist as a different crystal structure than the surface. The X-ray beam samples all phases from the surfaces to the center of the sample, and therefore the diffraction pattern can show lower-temperature phases than should be associated with the recorded temperature. This experimental artifact has been used to explain physically impossible results, such as the HCP+BCC+FCC data from Lin et al. (2002).

Diffraction of a liquid is significantly weaker than a solid phase, thus making the appearance of a melt difficult to verify. It is probable that the surfaces of the samples melted below the solidi shown on Figures 15 and 18, but that the weak melt peaks were completely overwhelmed by the strong solid peaks. Some previous experimenters have defined melting by the disappearance of solid phases (Shen et al.,

1998); however, the persistence of solid phases to over 3500 K (Figure 15) does not permit this method to be used for this study.

The temperature distribution model of Campbell et al. (2007) demonstrates that there could have been an axial temperature gradient of up to ~10% in the Fe-Si samples. That model showed a gradient of 10% for a sample 10 μm thick, a hot spot 30 μm across and a maximum temperature of 2000 K. Tighter focusing of the hot spot, or increasing the sample thickness could raise the thermal gradient. Unpublished data from Campbell (2009), based on the calculations reported in Campbell et al. (2007), indicates that a 10 μm thick sample with a hot spot 30 μm across will experience an average temperature 7% lower than the peak surface temperature in the volume sampled by a 6 μm -diameter x-ray beam.

The solidus for Fe-16Si based on XRD data is approximately 10% higher than the optically obtained curve. The solidus for Fe-9Si based on XRD data is estimated to be closer to 25% higher than the optically obtained curve; this may be due to extremely weak scattering of the melt phase, obfuscating the actual solidus at lower temperatures, or thick samples with molten surfaces and solid cores. It is also possible that the waist of the laser beam was tighter for the Fe-9Si samples. The two compositions absorbed the lasers with different efficiencies, so the laser intensity was adjusted to compensate.

4.4. The B2 Phase

If the temperatures are reduced by approximately 25% for Fe-9Si data, the phases shown in Figures 15 and 18 fit with earlier data from Lin et al. (2002, 2009). However, the B2 structure has not been previously reported for this composition. It is likely that B2 was seen by previous authors instead of BCC, but that the smaller, odd-numbered peaks were overlooked. It is possible that the HCP+BCC field reported by Lin et al. (2009) is, in fact, HCP+B2. Because of the difference in Gibbs free energy across the transition, thermodynamic models such as that of Brosh et al. (2009) should be re-evaluated to include the B2 structure.

Lin et al. (2002) drew the HCP / BCC+HCP transition as sharply curved between 40 GPa and 60 GPa (Figure 3). Based on data from this study, it appears that this apparent curve is the result of an invariant point where the BCC/B2 transition intersects the HCP / HCP+BCC transition (Figure 15). This point is probably located at ~58 GPa in accordance with the curve in Lin et al. (2002); its temperature is uncertain for reasons previously described, but on Figure 15 it has been estimated at 2400 K.

Because there is an increase in density across the BCC-B2 transition of $0.9\pm 0.1\%$, the possibility of the B2 structure in the inner core has implications for the silicon content in the core's composition. A denser structure would require a greater silicon content to account for the same density deficit. While Lin et al. (2009) concluded that an iron alloy with 8 wt.% silicon would likely be solely in the HCP structure at core conditions, they also note that the effect of adding Ni and other trace elements to the composition is unknown. Because the BCC/B2 phase disappears at low

temperatures, and because the temperature at the ICB is uncertain, it is unclear whether there could be B2 in an inner core with a composition close to Fe-9Si.

The B2 structure appears above 80 GPa in Fe-16Si from the melting curve down to at least 2000 K. This appears to be part of a high-pressure pattern of increasing stabilization of a body-centered cubic phase with silicon content, consistent with the pattern at 1 bar. Phase diagrams for pure iron (e.g. Shen et al., 1998) show limited BCC fields below 10 GPa (Figure 1). At 3-4 wt.% silicon, there is a limited field of coexisting BCC and HCP at 21 GPa and temperatures below 700 K (Lin et al, 2002; Asanuma, 2008) (Figure 3). At 9 wt.% silicon, BCC coexists with HCP up to at least 140 GPa at high temperatures (Lin et al, 2009). At 16 wt.% silicon, B2 exists alone at 82 GPa from 2000 K to 3000 K. Because the ICB is likely to be at high temperature (Alfe et al. [2003] calculated it to be at 6350 ± 500 K), the body-centered cubic phase in the inner core is likely to be B2 instead of BCC.

4.5. Silicon and the Density Deficit

It is possible to calculate the density of iron for an adiabatic transect of the outer core using the equation of state for HCP-Fe of Dewaele et al. (2006), an assumed temperature at the CMB and an assumed ΔV on melting of 1% or 2%. The Dewaele et al. (2006) equation of state has four components: isothermal compression is calculated using the Birch-Murnaghan equation (Equation 3); two terms account for harmonic and anharmonic vibrations according to the Debye model of solids, and an additional term accounts for the thermal contribution of electronic heat capacity. An adiabatic transect of the outer core was calculated using the equation:

$$[\delta \ln(T)/ \delta \ln(\rho)] = \gamma \quad (5)$$

In this equation, T is temperature, ρ is density and γ is the Grüneisen parameter, which is taken as a constant equal to 1.45 for the outer core (Anderson, 2002). The adiabat was calculated for densities between the CMB and ICB according to PREM (Dziewonski and Anderson, 1981), and these densities were converted to pressures using the equation of Dewaele et al. (2006).

Calculation of the density of iron allows easy comparison with a density model for the outer core such as PREM (Dziewonski and Anderson, 1981) (Figure 22). If it is concluded, based on the results of Figure 21, that the density of an iron-silicon alloy can be calculated from the iron equation of state simply by adjusting the mean atomic weight, then it is possible to calculate the amount of silicon necessary to satisfy the deficit between the HCP-Fe and PREM core densities (Figure 23). Errors for these curves are derived from differences in the curvature between the Dewaele et al. (2006) equation of state for iron and PREM density values for the outer core (Figure 24). For a CMB temperature of 4000 K, 8.6 wt.% to 11.1 wt.% silicon are required to satisfy the density deficit. A higher temperature at the CMB requires less silicon to satisfy the density deficit. This range depends on the ΔV of melting, error in the equation of state and error in PREM; a smaller ΔV of melting requires more to satisfy the density deficit.

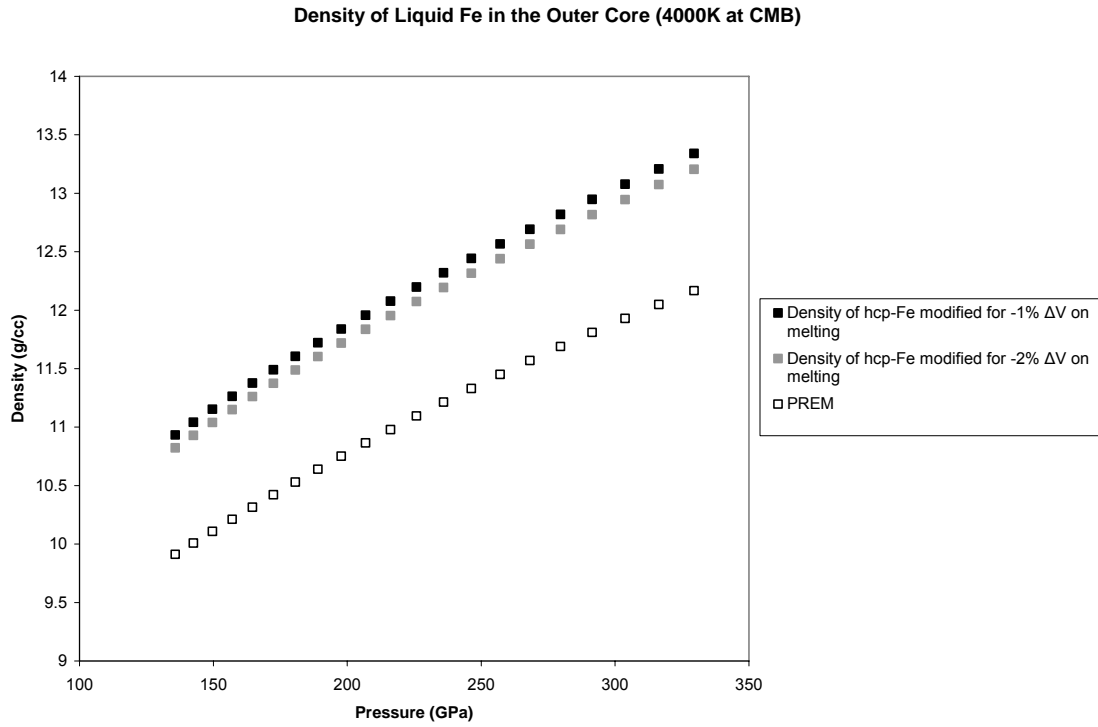


Figure 22. Calculated densities of liquid Fe using the equation of state of Dewaele et al., 2007 for HCP-Fe. The temperature at the CMB was assumed to be 4000 K. The open squares show densities from PREM (Dziewonski and Anderson, 1981).

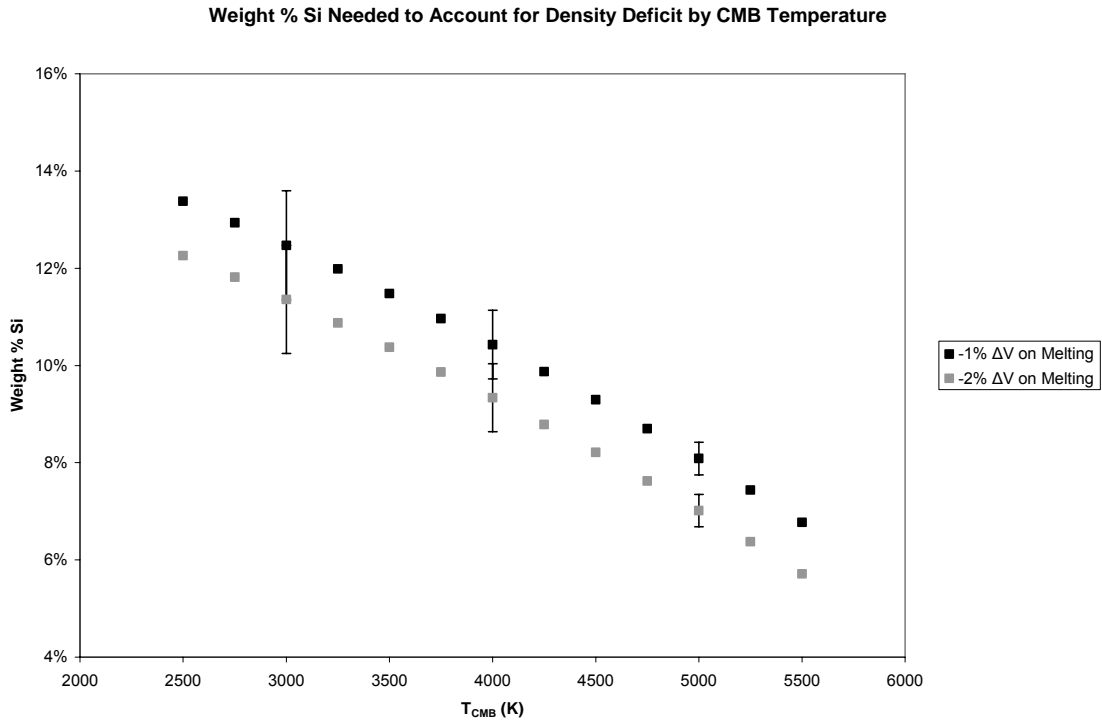


Figure 23. Calculated amounts of silicon necessary to satisfy the density deficit between HCP-Fe and PREM at a range of temperatures for the CMB. The calculations assume that the density deficit is due solely to the lighter mean atomic weight of the alloy, which is supported by Figure 19. An explanation of the error bars is shown in Figure 24.

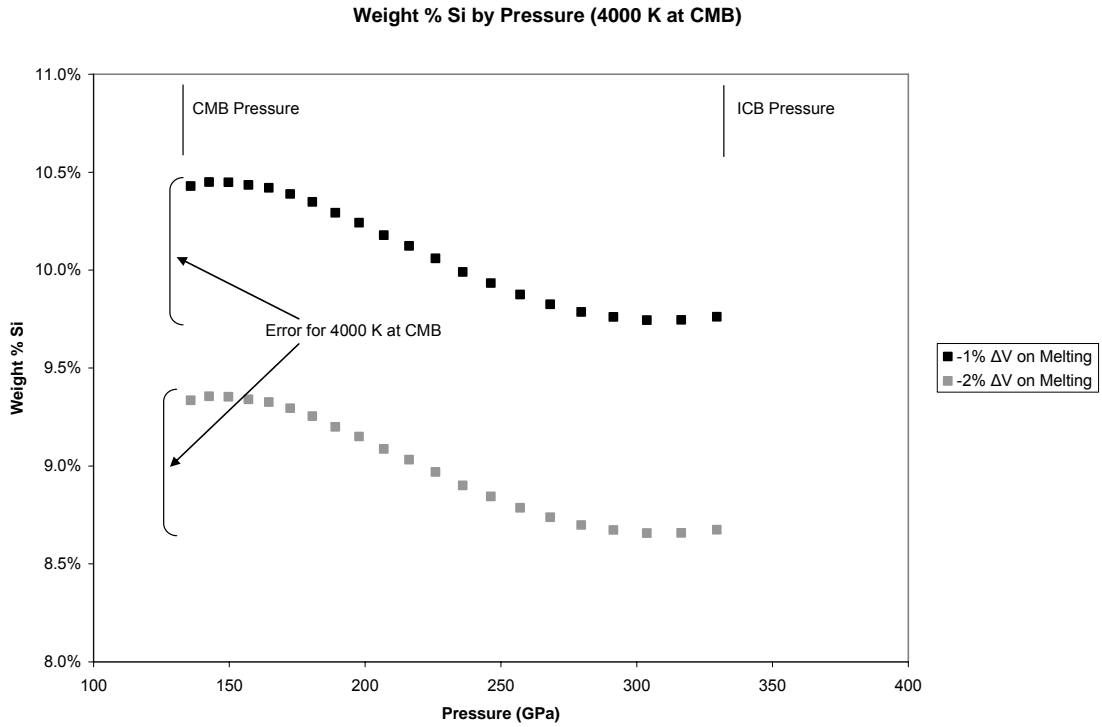


Figure 24. Error calculation for Figure 23. The curves show the amount of Si needed to satisfy the density deficit for an adiabatic profile through the outer core. Because the equation of Dewaele et al. (2006) does not have the same curvature as the PREM density model, the resulting curves are not constant. The error at this temperature is taken to be the difference between the maximum and minimum values for each curve.

Estimates for the temperature at the CMB center around 4000 K based on the melting temperature of iron at CMB pressures (Boehler, 1993). More recent studies of seismostratigraphy and the post-perovskite phase at the base of the mantle suggest that the temperature is in the range of 3700 K to 4000 K (Tateno et al, 2009; van der Hilst et al., 2007). The change in volume on melting of pure iron is estimated to be 1-2% (Belonoshko and Ahuja, 1997; Brown and McQueen, 1986). The amount of silicon needed to satisfy the density deficit is therefore approximately 10 wt.% (Figure 23).

4.6. Application to the Core

The melting depression for the Fe-Si alloys studied is small (~50 K at 21 GPa) compared to the depression in the Fe-O system (~ 200 K; Seagle et al., 2008) and Fe-S system (~800 K; Campbell et al., 2007) at similar pressures. If the small depression extends to core pressures, the addition of silicon could have a negligible effect on the freezing temperature of the inner core. Previous studies on Fe-Si alloys at megabar pressures (e.g. Lin et al., 2009) do not report melting temperatures.

If the small depression in melting temperature persists to core pressures, a silicon-bearing inner core would be very hot. This suggests that the core is cooling at a very slow rate, which could account for the small volume of the inner core. Data are required at higher pressures before a quantitative prediction of the core's thermal structure can be made.

It has been assumed previously that the core's density deficit can be attributed strictly to a mean atomic weight less than iron, with no volume change relative to pure iron (McDonough, 2003; Birch, 1966); this assumption is supported by data from this

study (Figures 21, 22 and 23). 8.6% to 11.1% Si would be necessary to satisfy the deficit for a CMB temperature of 4000 K. Seagle et al. (2006) showed that ~11% to 14% S would be necessary to satisfy the deficit at the same temperature.

McDonough (2003) proposed a core composition containing 6 wt.% silicon; according to Figure 23, this would require a CMB temperature of at least 5000 K. However, better constraints on the equation of state of iron at core pressures could raise or lower this temperature. A 1% change in the ΔV on melting affects the amount of silicon in the core by 1 wt.% (Figure 23). A 1000 K change in CMB temperature has double that effect. Consequently, in order to narrow down the composition of the core it would be most helpful to constrain the temperature at the CMB. It would be similarly beneficial to refine current equations of state for iron and density models of the outer core; this could reduce error on the calculation of the core's silicon content.

4.7. Future Work

While it appears that accurate melting temperatures have been obtained using optical methods, temperatures for sub-solidus data can be more accurately obtained in future experiments by using thinner samples. This may be possible with the use of finer-grained starting materials, although greater potential for oxidation exists for fine-grained ferrous materials due to the proportionally large surface area. It is especially important to determine which solid phase disappears at the Fe-9Si solidus, as this helps to determine the crystal structure of a Si-rich core.

If melting temperatures remain questionable based on XRD data, optical data obtained using the method of Campbell (2008) will provide an acceptable substitute.

The melting curves from this study should be extended to core pressures, and additional curves should be constructed for other Fe-Si compositions. It is important to verify that the curves do represent solidi and not liquidus. Refinement of the technique could produce information on sub-solidus phase transitions, which would serve to corroborate phase diagrams based on XRD data.

The phase diagrams for various Fe-Si compositions should be extended to core pressures. Lin et al. (2009) and Dubrovinsky et al. (2003) made some progress by compressing an alloy up to 240 GPa and 3300 K, but those studies produced no melting data. Most importantly, pressure-volume relationships should be obtained for various compositions in order to ascertain their densities under core conditions. Equations of state cannot be calculated from this study because of the multitude of phase transitions below 80 GPa.

5. Conclusions

- I. The addition of silicon lowers the melting point of iron by a smaller amount than the addition of similar amounts of sulfur or oxygen. The melting curves for Fe-9Si and Fe-16Si converge at ~ 50 GPa with a depression of ~ 150 K relative to pure iron. If this small depression extends to the Earth's core, a silicon-bearing core would be very hot and would be cooling at a very slow rate. This could explain the small size of the inner core.

- II. The phase diagrams for Fe-9Si and Fe-16Si are very different from each other and from the phase diagram of pure iron. Both are notable for the presence of the B2 structure at high pressures, which supports earlier hypotheses that a body-centered cubic phase is present in the inner core. Existing thermodynamic models should be re-evaluated to account for the B2 phase.

- III. Iron and silicon atoms compress by the same percentage at any given pressure up to at least 90 GPa. This supports earlier assumptions that the core's density deficit can be attributed to a difference in mean atomic weight relative to iron. It also allows calculation of the amount of silicon necessary to satisfy the density deficit for a range of CMB temperatures. With a CMB temperature of 4000 K, the core would contain 8.6 to 11.1 wt.% silicon.

6. Appendix

The following tables contain all of the data obtained from x-ray diffraction studies, including data measured directly at the beamline and data calculated from diffraction patterns. Table A shows data relating to FCC and HCP phases in Fe-9Si; Table B shows data relating to BCC and B2 in Fe-9Si; Table C shows data relating to all phases in Fe-16Si except Phase X. No information on Phase X is presented because its structure, density and other critical parameters are unknown. The following column heading abbreviations apply to all three tables:

T_m – Temperature measured and recorded at the beamline.

T_{NaCl} – Average temperatures experienced by the NaCl pressure medium.

$$T_{NaCl} = [(T_m - 300) \cdot 0.75] + 300 \quad (2)$$

T_{Fe} – Average temperature experienced by the sample in the volume sampled by the x-ray beam.

$$T_{Fe} = [(T_m - 300) \cdot 0.93] + 300 \quad (6)$$

V_c – Unit cell volume of Fe-Si alloy phase.

V_a – Average volume per atom of Fe-Si alloy phase.

ρ – Density of Fe-Si alloy of Fe-Si alloy phase.

ρ_{Fe} – Density of pure iron at identical conditions based on the equation of state of Dewaele et al. (2006).

$V_{a, Fe}$ – Average volume per atom of pure iron.

$V_a/V_{a, Fe}$ – Ratio of the atomic volumes of Fe-Si alloy phase to the atomic volume of pure iron.

In Table B, asterisks denote samples in which neither BCC nor B2 was found.

Table A:

Sample	Pressure	Pressure Error	Phase(s)	Tm	TNaCl	TFe	Vc	Vc Error	Va	Va Error	ρ	ρ Error	Fe ρ	Fe Va	Va/Va	Va/Va Error
S19_028	35.6	3.4	HCP+BCC	2000	1575	1881	20.287	0.023	10.143	0.012	8.927	0.010	9.188	10.093	1.005	0.001
S19_038	32.2	2.1	FCC+BCC	2078	1634	1954	41.715	0.807	10.429	0.202	8.683	0.168	9.049	10.248	1.018	0.020
S19_055	67.2	5.5	HCP	2066	1625	1942	18.936	0.048	9.468	0.024	9.564	0.024	10.063	9.215	1.027	0.003
S19_059	70.6	2.5	HCP+B2	2729	2122	2559	18.164	0.045	9.082	0.023	9.971	0.025	9.998	9.275	0.979	0.002
S19_060	70.3	1.4	HCP+B2	2760	2145	2588	18.723	0.021	9.361	0.011	9.673	0.011	9.984	9.288	1.008	0.001
S19_062	70.9	1.5	HCP+B2	3006	2330	2817	18.770	0.021	9.385	0.011	9.648	0.011	9.941	9.329	1.006	0.001
S19_063	70.8	3.3	HCP+B2	3091	2393	2896	19.092	0.020	9.546	0.010	9.486	0.010	9.917	9.351	1.021	0.001
S19_072	69.0	2.2	HCP	2660	2070	2495	19.550	0.045	9.775	0.023	9.264	0.021	9.976	9.296	1.052	0.002
S19_086	51.9	1.4	HCP+BCC	2500	1950	2346	20.116	0.022	10.058	0.011	9.003	0.010	9.556	9.704	1.036	0.001
S19_087	52.2	1.6	HCP+BCC	2678	2084	2512	20.390	0.023	10.195	0.011	8.882	0.010	9.515	9.746	1.046	0.001
S19_090	52.0	3.1	HCP+B2	2982	2312	2794	20.337	0.023	10.169	0.011	8.905	0.010	9.426	9.838	1.034	0.001
S19_104	59.1	3.1	HCP+B2	2461	1921	2310	19.073	0.022	9.537	0.011	9.495	0.011	9.765	9.497	1.004	0.001
S19_105	61.7	1.5	HCP+B2	2880	2235	2699	20.383	0.039	10.191	0.019	8.885	0.017	9.731	9.530	1.069	0.002
S19_106	62.5	1.5	HCP+B2	2991	2318	2803	19.776	0.021	9.888	0.011	9.158	0.010	9.724	9.537	1.037	0.001
S19_107	61.5	2.8	HCP+B2	3340	2580	3127	19.943	0.023	9.972	0.011	9.081	0.010	9.602	9.658	1.032	0.001
S19_108	62.6	1.8	HCP+B2	3487	2690	3264	19.851	0.022	9.925	0.011	9.123	0.010	9.591	9.669	1.027	0.001
S19_110	62.9	1.8	HCP+B2	3851	2963	3602	19.169	0.022	9.584	0.011	9.448	0.011	9.493	9.769	0.981	0.001
S19_188	44.3	1.6	HCP+BCC	2183	1712	2051	19.954	0.021	9.977	0.011	9.076	0.010	9.414	9.851	1.013	0.001
S19_189	44.8	1.4	HCP+BCC	2411	1883	2263	19.954	0.021	9.977	0.011	9.076	0.010	9.367	9.900	1.008	0.001
S19_190	45.2	1.4	HCP+BCC	2494	1946	2340	19.985	0.022	9.992	0.011	9.062	0.010	9.356	9.912	1.008	0.001
S19_192	46.3	1.9	FCC+B2	3179	2459	2977	20.760	0.022	10.380	0.011	8.724	0.009	9.186	10.095	1.028	0.001
S19_193	47.9	1.5	FCC+B2	3374	2606	3159	19.968	0.022	9.984	0.011	9.069	0.010	9.173	10.110	0.988	0.001
S19_205	45.6	1.6	HCP+BCC	2307	1805	2167	20.303	0.021	10.151	0.010	8.920	0.009	9.418	9.847	1.031	0.001
S19_210	46.2	1.8	FCC+B2	3053	2365	2860	20.070	0.022	10.035	0.011	9.024	0.010	9.222	10.056	0.998	0.001
S19_250	78.5	1.8	HCP	2254	1766	2117	18.735	0.021	9.367	0.011	9.667	0.011	10.290	9.012	1.039	0.001
S19_251	79.6	1.6	HCP	2457	1918	2306	18.955	0.021	9.477	0.011	9.554	0.011	10.274	9.026	1.050	0.001
S19_337	22.3	1.2	FCC+BCC	2006	1580	1887	43.079	0.354	10.770	0.088	8.408	0.069	8.697	10.663	1.010	0.008
S19_352	28.0	1.3	FCC+BCC	2263	1772	2126	45.180	1.808	11.295	0.452	8.017	0.321	8.835	10.496	1.076	0.043
S19_354	27.4	1.8	FCC+BCC	2410	1883	2262	42.665	0.182	10.666	0.046	8.489	0.036	8.760	10.586	1.008	0.004
S19_360	28.2	2.3	FCC+BCC	2688	2091	2521	42.560	0.262	10.640	0.065	8.510	0.052	8.688	10.674	0.997	0.006
S19_362	28.0	2.6	FCC+BCC	2947	2285	2762	42.598	0.410	10.649	0.102	8.503	0.082	8.577	10.812	0.985	0.009
S19_386	29.3	1.2	FCC+BCC	3048	2361	2856	42.482	0.190	10.621	0.047	8.526	0.038	8.592	10.793	0.984	0.004
S19_542	20.3	0.7	FCC+BCC	1541	1231	1454	43.411	0.017	10.853	0.004	8.344	0.003	8.769	10.575	1.026	0.000
S19_546	20.4	0.8	FCC+BCC	1646	1310	1552	43.642	0.085	10.910	0.021	8.300	0.016	8.740	10.610	1.028	0.002
S19_550	20.3	1.3	FCC+BCC	1786	1415	1682	43.869	0.048	10.967	0.012	8.256	0.009	8.688	10.674	1.027	0.001
S19_557	18.7	0.9	FCC+BCC	2042	1607	1920	44.461	0.537	11.115	0.134	8.147	0.098	8.504	10.905	1.019	0.012

Table B:

Sample	Pressure	Pressure Error	Phase(s)	Tm	TNaCl	TFe	Vc	Vc Error	Va	Va Error	ρ	ρ Error	Fe ρ	Fe Va	Va/Va	Va/Va Error
S19_028	35.6	3.4	HCP+BCC	2000	1575	1881	20.664	0.075	10.332	0.038	8.764	0.032	9.188	10.093	1.024	0.004
S19_038	32.2	2.1	FCC+BCC	2078	1634	1954	20.907	0.000	10.454	0.000	8.662	0.000	9.049	10.248	1.020	0.000
S19_055	67.2	5.5	HCP	2066	1625	1942	*									
S19_059	70.6	2.5	HCP+B2	2729	2122	2559	19.138	0.000	9.569	0.000	9.463	0.000	9.998	9.275	1.032	0.000
S19_060	70.3	1.4	HCP+B2	2760	2145	2588	18.803	0.033	9.401	0.017	9.632	0.017	9.984	9.288	1.012	0.002
S19_062	70.9	1.5	HCP+B2	3006	2330	2817	18.698	0.350	9.349	0.175	9.686	0.181	9.941	9.329	1.002	0.019
S19_063	70.8	3.3	HCP+B2	3091	2393	2896	19.289	0.499	9.645	0.249	9.389	0.243	9.917	9.351	1.031	0.027
S19_072	69.0	2.2	HCP	2660	2070	2495	*									
S19_086	51.9	1.4	HCP+BCC	2500	1950	2346	19.449	0.034	9.724	0.017	9.312	0.016	9.556	9.704	1.002	0.002
S19_087	52.2	1.6	HCP+BCC	2678	2084	2512	19.583	0.038	9.792	0.019	9.248	0.018	9.515	9.746	1.005	0.002
S19_090	52.0	3.1	HCP+B2	2982	2312	2794	19.974	0.018	9.987	0.009	9.067	0.008	9.426	9.838	1.015	0.001
S19_104	59.1	3.1	HCP+B2	2461	1921	2310	18.965	0.092	9.483	0.046	9.549	0.046	9.765	9.497	0.999	0.005
S19_105	61.7	1.5	HCP+B2	2880	2235	2699	19.426	0.000	9.713	0.000	9.323	0.000	9.731	9.530	1.019	0.000
S19_106	62.5	1.5	HCP+B2	2991	2318	2803	18.950	0.985	9.475	0.492	9.557	0.497	9.724	9.537	0.994	0.052
S19_107	61.5	2.8	HCP+B2	3340	2580	3127	19.660	0.068	9.830	0.034	9.212	0.032	9.602	9.658	1.018	0.003
S19_108	62.6	1.8	HCP+B2	3487	2690	3264	19.276	0.421	9.638	0.211	9.395	0.205	9.591	9.669	0.997	0.022
S19_110	62.9	1.8	HCP+B2	3851	2963	3602	19.131	0.000	9.565	0.000	9.467	0.000	9.493	9.769	0.979	0.000
S19_188	44.3	1.6	HCP+BCC	2183	1712	2051	19.884	0.044	9.942	0.022	9.108	0.020	9.414	9.851	1.009	0.002
S19_189	44.8	1.4	HCP+BCC	2411	1883	2263	20.220	0.129	10.110	0.065	8.957	0.057	9.367	9.900	1.021	0.007
S19_190	45.2	1.4	HCP+BCC	2494	1946	2340	20.115	0.024	10.057	0.012	9.003	0.011	9.356	9.912	1.015	0.001
S19_192	46.3	1.9	FCC+B2	3179	2459	2977	20.470	0.000	10.235	0.000	8.847	0.000	9.186	10.095	1.014	0.000
S19_193	47.9	1.5	FCC+B2	3374	2606	3159	19.925	0.000	9.963	0.000	9.089	0.000	9.173	10.110	0.985	0.000
S19_205	45.6	1.6	HCP+BCC	2307	1805	2167	19.982	0.027	9.991	0.014	9.063	0.012	9.418	9.847	1.015	0.001
S19_210	46.2	1.8	FCC+B2	3053	2365	2860	20.516	0.047	10.258	0.023	8.827	0.020	9.222	10.056	1.020	0.002
S19_250	78.5	1.8	HCP	2254	1766	2117	*									
S19_251	79.6	1.6	HCP	2457	1918	2306	*									
S19_337	22.3	1.2	FCC+BCC	2006	1580	1887	21.784	0.258	10.892	0.129	8.314	0.098	8.697	10.663	1.021	0.012
S19_352	28.0	1.3	FCC+BCC	2263	1772	2126	20.685	1.055	10.342	0.527	8.755	0.446	8.835	10.496	0.985	0.050
S19_354	27.4	1.8	FCC+BCC	2410	1883	2262	21.633	0.032	10.817	0.016	8.372	0.012	8.76	10.586	1.022	0.001
S19_360	28.2	2.3	FCC+BCC	2688	2091	2521	20.434	1.546	10.217	0.773	8.863	0.671	8.688	10.674	0.957	0.072
S19_362	28.0	2.6	FCC+BCC	2947	2285	2762	21.518	0.155	10.759	0.077	8.416	0.060	8.577	10.812	0.995	0.007
S19_386	29.3	1.2	FCC+BCC	3048	2361	2856	20.839	0.201	10.420	0.101	8.690	0.084	8.592	10.793	0.965	0.009
S19_542	20.3	0.7	FCC+BCC	1541	1231	1454	21.566	0.017	10.783	0.008	8.397	0.007	8.769	10.575	1.020	0.001
S19_546	20.4	0.8	FCC+BCC	1646	1310	1552	21.659	0.023	10.830	0.012	8.361	0.009	8.74	10.610	1.021	0.001
S19_550	20.3	1.3	FCC+BCC	1786	1415	1682	20.396	0.000	10.198	0.000	8.879	0.000	8.688	10.674	0.955	0.000
S19_557	18.7	0.9	FCC+BCC	2042	1607	1920	22.285	0.043	11.143	0.021	8.127	0.016	8.504	10.905	1.022	0.002

Sample	Pressure	Pressure Error	Phase(s)	Tm	TNaCl	TFe	Vc	Vc Error	Va	Va Error	ρ	ρ Error	Fe ρ	Fe Va	Va/Va	Va/Va Error
SI16_009	65.0	1.7	B2+X	1756	1392	1654	18.533	0.031	9.267	0.015	8.641	0.014	10.072	9.207	1.006	0.002
SI16_011	66.2	1.5	B2+X	2157	1693	2027	18.567	0.037	9.283	0.019	8.626	0.017	10.018	9.257	1.003	0.002
SI16_012	66.8	1.5	B2+X	2326	1820	2184	18.530	0.087	9.265	0.043	8.643	0.041	9.996	9.277	0.999	0.005
SI16_013	66.9	1.5	B2+X	2499	1949	2345	18.576	0.081	9.288	0.040	8.621	0.037	9.959	9.312	0.997	0.004
SI16_016	68.1	1.8	B2+X	2850	2213	2672	18.678	0.154	9.339	0.077	8.574	0.071	9.908	9.360	0.998	0.008
SI16_017	67.8	1.9	Melt	3036	2352	2844										
SI16_018	68.0	1.7	Melt	3130	2423	2932										
SI16_036	74.0	1.9	B2+X	2143	1682	2014	18.196	0.017	9.098	0.008	8.801	0.008	10.209	9.084	1.002	0.001
SI16_038	76.0	1.8	B2+X	2790	2168	2616	18.240	0.052	9.120	0.026	8.780	0.025	10.116	9.167	0.995	0.003
SI16_039	76.0	1.5	Melt	3038	2354	2846										
SI16_040	76.0	2.0	Melt	3105	2404	2909										
SI16_058	58.0	1.4	Melt	2862	2222	2683										
SI16_060	57.9	1.8	Melt	2987	2315	2799										
SI16_146	28.5	1.4	HCP	2142	1682	2013	20.868	0.026	10.434	0.013	7.674	0.010	8.895	10.426	1.001	0.001
SI16_154	25.0	1.4	BCC	2501	1951	2347	21.852	0.080	10.926	0.040	7.329	0.027	8.627	10.749	1.016	0.004
SI16_155	29.1	2.0	Melt	2685	2089	2518										
SI16_337	88.1	1.8	B2	2063	1622	1940	17.606	0.035	8.803	0.018	9.096	0.018	10.536	8.802	1.000	0.002
SI16_342	89.6	1.5	B2	2500	1950	2346	17.664	0.042	8.832	0.021	9.066	0.021	10.484	8.845	0.998	0.002
SI16_343	89.5	1.7	B2	2883	2237	2702	17.752	0.032	8.876	0.016	9.021	0.016	10.405	8.913	0.996	0.002
SI16_347	91.6	2.0	B2	3105	2404	2909	17.850	0.179	8.925	0.089	8.972	0.090	10.403	8.914	1.001	0.010
SI16_408	21.7	1.2	BCC	2280	1785	2141	21.512	0.015	10.756	0.008	7.445	0.005	8.568	10.823	0.994	0.001
SI16_411	21.5	1.2	BCC	2463	1922	2312	21.591	0.117	10.796	0.058	7.417	0.040	8.488	10.925	0.988	0.005
SI16_413	22.2	1.5	Melt	2700	2100	2532										
SI16_414	22.3	1.2	Melt	2887	2240	2706										
SI16_432	47.3	1.5	HCP	2188	1716	2056	19.479	0.015	9.739	0.008	8.222	0.006	9.502	9.760	0.998	0.001
SI16_435	49.2	2.3	BCC	2619	2039	2457	19.818	0.007	9.909	0.003	8.081	0.003	9.445	9.818	1.009	0.000
SI16_436	50.3	1.5	Melt	2872	2229	2692										
SI16_438	50.0	1.7	Melt	2715	2111	2546										

Table C:

7. References

- Alfe D., Gillan M. J. and Price G. D. (2003) Thermodynamics from first principles: Temperature and composition of the Earth's core. *Mineral. Mag.* 67, 113-123.
- Allegre C. J., Poirier J.-P., Humler E. and Hofmann A. W. (1995) The chemical composition of the Earth. *Earth Planet. Sci. Lett.* 134, 515-526.
- Anderson O. L. and Isaak D. G. (2002) Another look at the core density deficit of Earth's outer core. *Phys. Earth Planet. Int.* 131, 19-27.
- Anderson O. L. (2002) The power balance and the core-mantle boundary. *Phys. Earth Planet. Int.* 131, 1-17.
- Anderson W. W. and Ahrens T. J. (1994) An equation-of-state for liquid iron and implications for the Earth's core. *J. Geophys. Res.* 99, 4273-4284.
- Andrault D., Fiquet G., Charpin T. and le Bihan, T. (2000) Structure analysis and stability field of β -iron at high P and T. *Amer. Mineral.* 85, 364-371.
- Asahara Y., Frost D. J. and Rubie D. C. (2007) Partitioning of FeO between magnesiowustite and liquid iron at high pressures and temperatures: Implications for the composition of the Earth's outer core. *Earth Planet. Sci. Lett.* 257, 435-449.
- Asanuma H., Ohtani E., Sakai T., Terasaki H., Kamada S., Hirao N., Sata N. and Ohishi Y. (2008) Phase relations of Fe-Si alloy up to core conditions: Implications for the Earth inner core. *Geophys. Res. Lett.* 35, L12307.
- Badro J., Fiquet G., Guyot F., Gregoryanz E., Occelli F., Antonangeli D. and d'Astuto M. (2007) Effect of light elements on the sound velocities in solid iron: Implications for the composition of Earth's core. *Earth Planet. Sci. Lett.* 254, 233-238.
- Belonoshko A. B., Ahuja R. and Johansson B. (2003) Stability of the body-centred-cubic phase of iron in the Earth's inner core. *Nature* 424, 1032-1034.
- Belonoshko A. B., Skorodumova N. V., Rosengren A. and Johansson B. (2008) Elastic anisotropy of Earth's inner core. *Science* 319, 797-800.
- Belonoshko A. B. and Ahuja R. (1998) Embedded-atom molecular dynamic study of iron melting. *Phys. Earth Planet. Inter.* 102, 171-184.
- Birch F. (1952). Elasticity and constitution of the Earth's interior. *J. Geophys. Res.* 57, 227-286.
- Birch F. (1966) Evidence from high-pressure experiments bearing on density and composition of Earth. *Geophys. J. Roy. Astro. Soc.* 11, 256.

- Boehler R. (1993) Temperatures in the Earth's core from melting-point measurements of iron at high static pressures. *Earth Planet. Sci. Lett.* 111, 217-227.
- Boehler R., Ross M. and Boercker D. B. (1996) High-pressure melting curves of alkali halides. *Phys. Rev. B* 53, 556-563.
- Boehler R., Vonbargen N. and Chopelas A. (1990) Melting, thermal-expansion, and phase-transitions of iron at high-pressures. *J. Geophys. Res.* 95, 21731-21736.
- Boehler R. (1986) Experimental constraints on melting conditions relevant to core formation. *Geo. Cosmo. Acta* 60, 1109-1112.
- Brosh E., Makov G. and Shneck R. Z. (2009) Thermodynamic analysis of high-pressure phase equilibria in Fe-Si alloys, implications for the inner-core. *Phys. Earth Planet. Iner.* 172, 289-298.
- Brown J. M. and McQueen R. G. (1986) Phase transitions, Gruneisen parameter and elasticity for shocked iron between 77 GPa and 400 GPa. *J. Geophys. Res.* 91, 7485-7494.
- Campbell A. (2008) Measurement of temperature distributions across laser-heated samples of multispectral imaging radiometry. *Rev. Sci. Instrum.* 79, 015108.
- Campbell A. J., Danielson L., Richter K., Seagle C. T., Wang Y. and Prakapenka V. B. (2009) High pressure effects on the iron-iron oxide and nickel-nickel oxide oxygen fugacity buffers. *Earth Planet. Sci. Lett.*, submitted.
- Campbell A. J., Seagle C. T., Heinz D. L., Shen G. and Prakapenka V. B. (2007) Partial melting in the iron-sulfur system at high pressure: A synchrotron X-ray diffraction study. *Phys. Earth Planet. Int.* 162, 119-128.
- Canup R. M. and Asphaug E. (2001) Origin of the Moon in a giant impact near the end of the Earth's formation. *Nature* 412, 708-712.
- Corgne A., Keshav S., Wood B. J., McDonough W. F., and Fei Y. (2008) Metal-silicate partitioning and constraints on core composition and oxygen fugacity during Earth accretion. *Geochim. Cosmochim. Acta* 72, 574-589.
- Decker D. L. (1971) High-pressure equation of state for NaCl, KCl, and CsCl. *J. App. Phys.* 42, 3239-3244.
- Dewaele A., Fiquet G., Andrault D. and Hausermann D. (2000) P-V-T equation of state of periclase from synchrotron radiation measurements. *J. Geophys. Res.* 105, 2869-2877.
- Dewaele A., Loubeyre P. and Mezouar M. (2004) Equations of state of six metals above 94 GPa. *Phys. Rev. B* 70, 094112.

- Dewaele A., Loubeyre P., Occelli F., Mezouar M., Dorogokupets P. I. and Torrent M. (2006) Quasihydrostatic Equation of State of Iron above 2 Mbar. *Phys. Rev. Lett.* 97, 215504.
- Dreibus G. and Palme H. (1996) Cosmochemical constraints on the sulfur content in the Earth's core. *Geochim. Cosmochim. Acta* 60, 1125-1130.
- Dubrovinsky L., Dubrovinskaia N., Langenhorst F., Dobson D., Rubie D., Geßmann C., Abrikosov I. A., Johansson B., Baykov V. I., Vitos L., Le Bihan T., Crichton W. A., Dmitriev V. and Weber H.-P. (2003) Iron-silica interaction at extreme conditions and the electrically conducting layer at the base of the Earth's mantle. *Nature* 422, 58-61.
- Dziewonski A. and Anderson D.L. (1981) Preliminary reference Earth model. *Phys. Earth Planet. Inter.* 25, 297-356.
- Fei Y., Ricolleau A., Frank M., Mibe K., Shen G. and Prakapenka V. (2007) Toward an internally consistent pressure scale. *Proc. Nat. Acad. Sci.* 104, 9812-9816.
- Fischer R. A. and Campbell, A. J. (2009) Phase diagram of wüstite at high pressures and temperatures. *Geophys. Res. Lett.*, submitted.
- Hammersley A. P., Svensson S. O., Hanfland M., Fitch A. N. and Hausermann D. (1996) Two-dimensional detector software: From real detector to idealized image or two-theta scan. *High Pres. Res.* 14, 235-248.
- Heinz D. L. and Jeanloz R. (1987) in *High-Pressure Research in Mineral Physics*, edited by M. H. Manghnani and Y. Syono (American Geophysical Union, Washington DC).
- Jeanloz, R. (1987) Composition of the inner core. *Nature* 325, 303.
- Jephcoat A. and Olson P. (1987) Is the inner core of the Earth pure iron? *Nature* 325, 332-335.
- Lazor P., Shen G. and Saxena S. K. (1993) Laser-heated diamond anvil cell experiments at high pressure; melting curve of nickel up to 700 kbar. *Phys. Chem. Min.* 20, 86-90.
- Lee C.-T. A., Yin Q., Lenardic A., Agranier A., O'Neill C. J., and Thiagarajan N. (2007) Trace-element composition of Fe-rich residual liquids formed by fractional crystallization: Implications for the Hadean magma ocean. *Geo. Cosmo. Acta* 71, 3601-3615.
- Knopoff L. and MacDonald J. G. F. (1960) An equation-of-state for the core of the Earth. *Geophys. J. R. Astron. Soc.* 3, 68-77.

- Kuwayama Y. and Hirose K. (2004) Phase relations in the system Fe-FeSi at 21 GPa. *Amer. Mineral.* 89, 273-276.
- MacDonald G. J. F. and Knopoff L. (1958) On the chemical composition of the outer core. *Geophys. J.* 1, 284-297.
- Mao, H.-K., J. Xu, and P. M. Bell (1986), Calibration of the ruby pressure gauge to 800 kbar under quasi-hydrostatic conditions, *J. Geophys. Res.* 91, 4673-4676.
- Mao H. K., Bell P. M. and Hadidiacos C. (1987) Experimental phase relations of iron to 360 kbar, 1400 degrees C, determined in an internally heated diamond-anvil apparatus. In *High Pressure Research in Mineral Physics* (Manghnani, M. H., ed., University of Hawaii at Manoa, Honolulu).
- Massalski T. B., ed. in chief (1986) *Binary Alloy Phase Diagrams* (American Society for Metals, Metals Park, OH).
- Masters G. and Gubbins D. (2003) On the resolution of density within the Earth. *Phys. Earth Planet. Int.* 140 159-167.
- McDonough W. F. (2003) Compositional model for the Earth's core. In *Treatise on Geochemistry*, v. 2 (ed. R. W. Carlson). Elsevier-Pergamon, Oxford, 547-568.
- McQueen R. G. and Marsh S. F. (1966) Shock wave compression of iron-nickel alloys and the Earth's core. *J. Geophys. Res.* 71, 1751-1756.
- O'Neill H. S., Canil D. and Rubie D. C. (1998) Oxide-metal equilibria to 2,500 degrees C and 25 GPa: Implications for core formation and the light component in the Earth's core. *J. Geophys. Res.* 103, 12239-12260.
- Ozawa H., Hirose K., Mitome M., Bando Y., Sata N. and Ohishi Y. (2008) Chemical equilibrium between ferropericalse and molten iron to 134 GPa and implications for iron content at the bottom of the mantle. *Geophys. Res. Lett.* 35.
- Prakapenka V. B., Kubo A., Kuznetsov A., Laskin A., Shkurikhin O., Dera P., Rivers M. L. and Sutton S. R. (2008) Advanced flat top laser heating system for high pressure research at GSECARS: Application to the melting behavior of germanium. *High Pres. Res.* 28, 225-235.
- Righter K., Drake M. J. and Yaxley, G. (1997) Prediction of siderophile element meta-silicate partition coefficients to 20GPa and 2800°C: the effects of pressure, temperature, oxygen fugacity, and silicate and metallic melt compositions. *Phys. Earth Planet. Inter.* 100, 115-134.
- Rubie D. C., Melosh H. J., Reid J. E., Liebske C., and Righter K. (2003) Mechanisms of metal-silicate equilibration in the terrestrial magma ocean. *Earth Planet. Sci. Lett.* 205, 239-255.

- Seagle C. T., Campbell A. J., Heinz D. L., Shen G. and Prakapenka V. B. (2006) Thermal equation of state of Fe₃S and implications for sulfur in Earth's core. *J. Geophys. Res.* 111, B06209.
- Seagle C. T., Heinz D. L., Campbell A. J., Prakapenka V. B. and Wanless S. T. (2008) Melting and thermal expansion in the Fe-FeO system at high pressure. *Earth Planet. Sci. Lett.* 265, 655-665.
- Shanker J., Singh B. P. and Srivastava S. K. (2004) Volume-temperature relationship for iron at 330 GPa and the Earth's core density deficit. *Phys. Earth Planet Int.* 147, 333-341.
- Shen G., Mao H. K., Hemley R. J., Duffy T. S., Rivers M. L. (1998) Melting and crystal structure of iron at high pressures and temperatures. *Geophys. Res. Lett.* 25, 373-376.
- Shen G. Y., Prakapenka V. B., Eng P. J., Rivers M. L. and Sutton S. R. (2005) Facilities for high-pressure research with the diamond anvil cell at GSECARS. *J. Synch. Rad.* 12, 642-649.
- Shen G. Y., Rivers M. L., Wang Y. B. and Sutton S. R. (2001) Laser heated diamond anvil cell system at the Advanced Photon Source for in situ x-ray measurements at high pressure and temperature. *Rev. Sci. Instrum.* 72, 1273-1282.
- Stevenson D. J. (2003) Planetary magnetic fields. *Earth Planet. Sci. Lett.* 208, 1-11.
- Tateno S., Hirose K., Sata N. and Ohishi Y. (2009) Determination of post-perovskite phase transition boundary up to 4000 K and implications for thermal structure in D'' layer. *Earth Planet. Sci. Lett.* 277, 130-136.
- van der Hilst R. D., de Hoop M. V., Wang P., Shim S.-H., Ma P. and Tenorio L. (2007) Seismostratigraphy and thermal structure of Earth's core-mantle boundary. *Science* 30, 1813-1817.
- Vocadlo L., Alfe D., Gillan M. J. and Price G. D. (2003) The properties of iron under core conditions from first principles calculations. *Phys. Earth Planet. Int.* 140, 101-125.
- Wood B. J. (2003) Carbon in the core. *Earth Planet. Sci. Lett.* 117, 593-607.
- Wood B. J., Wade J., and Kilburn M. R. (2007) Core formation and the oxidation state of the Earth: Additional constraints from Nb, V and Cr partitioning. *Geochim. Cosmochim. Acta* 72, 1415-1426.
- Yoshino T., Walter M. J. and Katsura T. (2004) Connectivity of molten iron alloy in peridotite based on in situ electrical conductivity measurements: implications for core formation in terrestrial planets. *Earth Planet. Sci. Lett.* 222, 625-643.

Zhang J. and Guyot F. (1999) Experimental study of the bcc-fcc phase transformations in the Fe-rich system Fe-Si at high pressures. *Phys. Chem. Minerals* 26, 419-424.